Everyday Electromechanics: Capacitive strong coupling to mechanical motion

by

Denise Puglia

August, 2024

A thesis submitted to the
Graduate School
of the
Institute of Science and Technology Austria
in partial fulfillment of the requirements
for the degree of
Doctor of Philosophy

Committee in charge:

Robert Seiringer, Chair
Andrew Higginbotham
Georgios Katsaros
Silvan Schmid

The thesis of Denise Puglia, titled *Everyday Electromechanics: Capacitive strong coupling to mechanical motion*, is approved by:

Supervisor: Andrew Higginbotham, ISTA, Klosterneuburg, Austria

Signature: ____________________

Committee Member: Georgios Katsaros, ISTA, Klosterneuburg, Austria

Signature: ____________________

Committee Member: Silvan Schmid, Institute of Sensor and Actuator Systems, TU Wien, Austria

Signature: ____________________

Defense Chair: Robert Seiringer, ISTA, Klosterneuburg, Austria

Signature: ____________________

Signed page is on file

© by Denise Puglia, August, 2024
CC BY-NC 4.0 The copyright of this thesis rests with the author. Unless otherwise indicated, its contents are licensed under a Creative Commons Attribution-NonCommercial 4.0 International License. Under this license, you may copy and redistribute the material in any medium or format. You may also create and distribute modified versions of the work. This is on the condition that: you credit the author and do not use it, or any derivative works, for a commercial purpose.

ISTA Thesis, ISSN: 2663-337X

I hereby declare that this thesis is my own work and that it does not contain other people's work without this being so stated; this thesis does not contain my previous work without this being stated, and the bibliography contains all the literature that I used in writing the dissertation.

I accept full responsibility for the content and factual accuracy of this work, including the data and their analysis and presentation, and the text and citation of other work.

I declare that this is a true copy of my thesis, including any final revisions, as approved by my thesis committee, and that this thesis has not been submitted for a higher degree to any other university or institution.

I certify that any republication of materials presented in this thesis has been approved by the relevant publishers and co-authors.

Signature: ______________________________

Denise Puglia
August, 2024

Signed page is on file

Abstract

We introduce a new all-electric platform, that strong couples light to mechanical motion by ensuring that the external environmental coupling dominates over internal mechanical dissipation. The system only has three everyday components: AC, DC, and a flip-chip, in which a metallized silicon nitride membrane is flipped on top of the device under test. This everyday electromechanical device can be operated at low or room temperature and has 10000× lower insertion loss than a comparable commercial quartz crystal, achieves a position imprecision matching state-of-the-art optical interferometer, and enables remote cooling of mechanical motion. The spatial properties of higher order mechanical modes are a promising feature for reconstructing unknown charge distributions.

Acknowledgements

I would like to thank all professors, friends, and colleagues that inspired, supported, and encouraged me during this last 5 years. I am very grateful to my advisor, Prof. Andrew Higgimbotham, for embarking on this adventure of developping a new measurement technique with me. A special thanks goes to Rachel, for making the day-to-day of electrical measurements lighthearted and funny, and to Niklas and Silvan, for showing me how to make membranes and fighting for my access to their cleanroom. I am grateful for the help from the Miba Machine Shop and Nanofabrication facility at IST Austria, the finantial support from the Austrian FWF grant P33692-N, and the DOC Fellowship of the Austrian Academy of Sciences (DOC – No. 26088).

As the PhD project did not work for the first 2,5 years, I had to bitterly learn that my life is not my work. For their support and eternal patience to hear me venting about my project, I give special credit to Manas, Barbara, Misha, the whole team Fljac, and Sybele. For his companionship and making the days of homeoffice very pleasant, I thank my partner André. Finally, as thanking one's parents has no age limit, I am very very grateful (one very is not enough) for my mom and dad for their unconditional love, support, and endless supply of entertainement and distraction. To everyone my "Muito Obrigada"!

About the Author

Denise Puglia completed a BSc in Engineering Physics at the Universidade Federal do Rio Grande do Sul (UFRGS) with a one year exchange at the University of California Berkeley. The Bachelor thesis focused on implementing a dual-tip magnetic force microscopy, while the internship aimed to develop a beam position monitor for Carnauba beamline of the synchrotron SIRIUS. In 2017 she joined the University of Copenhagen for a Msc in experimental condensed matter physics, while she worked as a cleanroom junior assistant. For the master thesis, she worked on the Microsoft project that aims to build a quantum computer based on majorana qubits. At ISTA, she focused her research on MEMS, presenting her work on several conferences on this field. Denise also joined a science education project and briefly eplored the field of bioMEMS.

List of Collaborators and Publications

This thesis contains the following preprint: Denise Puglia, Rachel Odessey, Peter S Burn, Niklas Luhmann, Silvan Schmid, and Andrew P Higginbotham. Everyday electromechanics: Capacitive strong coupling to mechanical motion. *arXiv preprint arXiv:2407.15314*, 2024.

The following publication is not included in this thesis, but it is a result of scientifc collaborations at ISTA during my PhD: Soham Mukhopadhyay, Jorden Senior, Jaime Saez-Mollejo, Denise Puglia, Martin Zemlicka, Johannes M Fink, and Andrew P Higginbotham. Superconductivity from a melted insulator in josephson junction arrays. *Nature Physics*, 19(11):1630–1635, 2023.

Table of Contents

Abstract vii

Acknowledgements viii

About the Author ix

List of Collaborators and Publications x

Table of Contents xi

List of Figures xii

1 Introduction 1

2 Theoretical Background 3
- 2.1 Continuum model . . . 4
- 2.2 Collapse physics . . . 6
- 2.3 Dynamics . . . 6
- 2.4 Coupling to a circuit . . . 7
- 2.5 Parametric gain . . . 11
- 2.6 Converting 2-port measurement into 1-port measurement . . . 15
- 2.7 Noise Temperature . . . 17

3 Design Simulation 19
- 3.1 Dynamic deflection of the Membrane . . . 19
- 3.2 Static deflection of the membrane . . . 20
- 3.3 Flip-Chip design . . . 20
- 3.4 Sonet Simulations . . . 21

4 Fabrication Techniques 23
- 4.1 Flip-Chip Fabrication . . . 23
- 4.2 Fabrication Techniques . . . 25

5 Measurement setup and non-everyday results 29
- 5.1 S-Parameters . . . 29
- 5.2 Parametric amplification . . . 30

6 Everyday Electromechanics at the fundamental mode 35

7 Everyday Electromechanics at the high order modes 45
- 7.1 Charge Distributions . . . 45

7.2 Multimode Measurements 47

8 Conclusion **51**

Bibliography **53**

A Calculating static displacement with Mathematica **61**

B Sample parameters **63**

List of Figures

2.1 (a) potential energy by plate separation with a static applied voltage. Note that as a larger static bias is applied, the minimum becomes increasingly unstable. (b) equilibrium value of x by applied voltage. 6

2.2 Two possible configurations for a one-port measurement. (a) Using a power splitter to add reflected and transmitted components. (b) Using a hybrid coupler to subtract reflected and transmitted components. 15

3.1 (a-d) Comsol simulation of the mode shape from a square membrane for modes (1,1), (2,1), (2,2), and (3,1). (e-f) Hybrid modes simulated by comsol at the eigenfrequencies from modes (4,2) and (2,4). (g) Sine-like mode (2,4) (h) Sum 1:1 of the sine-like modes (2,4) and (4,2) (i) Static deflection of a 500 μm membrane under $V_{\mathrm{DC}} = 1$ as calculated with Mathematica. 20

3.2 (a) Comsol simulation of the bending of the top chip due to the cooling to liquid nitrogen temperatures. The center of the chip is located at the left edge, while the stycast is placed on the bottom edge. (b) Electrode geometry considered for the simulation of scattering parameter S_{21} along the electrode. (c) Scattering parameter S_{21} along the electrode simulated with Sonnet. Such electrode would be flipped under a 500 μm membrane. 21

4.1 Fabrication process of a flip-chip. Membrane Fabrication: (i) high-resistivity silicon is covered in Si_3N_4, (ii) photolithography exposes a window which defines the membrane size, (iii) Si_3N_4 is etched with RIE, (iv) photolithography and RIE are used to remove Si_3N_4 from the front side, defining the area of the posts and the membrane, (v) KOH etches the silicon, and (vi) the membrane is metallized with gold. Electrode Fabrication: (vii) high-resistivity silicon is used as substrate, (viii) photolitography exposes the regions for the posts, (ix) posts are evaporated, (x) a second photolithography exposes the region for the electrode, (xi) the electrode is evaporated, and the wafer is dices and cleaned. (xii) The membrane chip is flipped on top of the electrode. 24

4.2 E-beam evaporation. (a) Dark field optical images of platinum on the electrode at 0.2 nm/s evaporation rate with the formation of Hillock grains (shown in the inset) and (b) at 0.1 nm/s without Hillock grains. (c) SEM of gold on the membrane at 25 deg evaporation angle. (d) Resistance across the step between region 1 and 2 as a function of evaporation angle. The inset shows the metal along the step for an evaporation angle of 30 deg. 27

4.3 (a) Top view of a flip-chip taken with an optical microscope. A quarter electrode is seen as yellow in the middle while the silicon substrate appears in pink. (b) Separation distance infered from the interference between the membrane and the electrode. (c) Filmetrics reflectance meaurement in blue and fit for the thickness of the air layer in red. (d) PCB with two flip-chips ready to be loaded into the measuring chamber. 28

5.1 (a) Circuit diagram in transmission mode. (b) Scattering parameter S_{21} measured in transmission mode with a Lorentian fit. (c) Circuit diagram in reflection mode. (d) Scattering parameter S_{11} measured in reflection mode and an inset showing the imaginary and real components of S_{11}. A circular fit to these components allows us to obtain the circuit parameters. 30

5.2 (a) Scattering parameter S_{21} measured in transmission mode for the measuring device being at high input impedance and at 50 Ω. (b) Demodulated X and Y time traces taken at high input impedance. (c) Demodulated X and Y quadratures with gain on and off taken at high input impedance. The solid line indicates 5$\times$ the variance of the data. 31

5.3 (a) Scattering parameter S_{11} as a function of frequency and ellapsed time. (b) Cryostat temperature as a function of time. (c) Voltage trace as a function of time for the amplified quadrature. (d) Mechanical Temperature with cryostat at LN temperature and a reference resistor at LN or RT. The black marker indicates the trace shown in (c). 32

6.1 **Everyday electromechanics (EEM) setup.** A metallized $\mathrm{Si_3N_4}$ membrane chip is flipped on an electrode chip and both are coupled to transmission lines, allowing the transmission S_{21} to be measured. The front left quadrant of the membrane chip is omitted from the schematics and only the contour lines are shown. A DC bias tunes the coupling between the transmission lines and the flipped chip. . 37

6.2 **Tuning from weak to strong electromechanical regime. a**, S_{21} transmission parameter around resonance for different voltages. The dashed green line indicates expected threshold transmission when the device is operated in the strong coupling regime $2g > \kappa_{\mathrm{in}}$. **b**, External coupling g and internal coupling κ_{in} as a function of voltage. Green marker was calculated from the highlighted trace in **a**. The full lines represent the voltage dependence fits. **c**, Cooperativity $\mathscr{C}$ as a function of voltage, with the green marker calculated from the highlighted trace in **a**. The dashed green line shows $\mathscr{C} = 1$, above which the device is considered to operate in the strong coupling regime. The full line indicates the expected cooperativity based on the voltage dependence fit from **b**, while the dotted line indicates the expected cooperativity for a constant internal coupling. 38

6.3 **Comparison with a commercial device.** **a**, S_{21} around the resonance and antiresonance for the crystal and the EEM at $\mathrm{V_{DC}} = 1$ V. Full line represents a fit. **b**, Antiresonance Ω_a and resonance Ω_m voltage dependence. The full line represents a fit of the voltage dependence from the mechanical resonance and expected antiresonance dependence based on this fit. **c**, Inductor quality factor Q_L data (marker) and fit (full line). The inset shows the commercial quartz crystal (CC1V-T1A) resonance. **d**, Inductive bandwidth BW_L, defined by the frequency range over which $\mathrm{Im}(Z) > 0$ for a fixed $V_{\mathrm{DC,S}}$. Points are calculated from the data in **c**, and the line is a guide to the eye. Horizontal line indicates inductive bandwidth of the crystal. 40
6.4 **High-precision position measurements.** **a**, demodulated X and Y quadratures for EEM with (orange) and without (green) parametric gain. The full line represents 4x the standard deviation of the data. **b**, the voltage spectral density S_{VV} for the parametrically amplified trace shown in **a**. The solid line is a fit to a Lorentzian with an offset bg (dotted line). The green shading indicates the voltage noise of the measurement amplifier and the orange shading indicates the excess noise due to thermomechanical fluctuations. **c**, Position imprecision inferred from **b** using Eq. 6.8. The full gray line represents the expected contribution of thermomechanical fluctuations at 295 K. 41
6.5 **Back-action isolation.** **a**, EEM circuit in reflection and back-action isolation mode. The temperature of the external port is determined by a 50 Ω resistor at LN (ice cube) or room (fire) temperature. **b**, Voltage spectral density for an EEM device thermalized to RT and LN. The full line represents a Lorentzian curve as a guide to the eye. The thermomechanical fluctuations are proportional to the area between the trace and the background, as indicated by the shading. **c**, Area under the curve of the thermomechanical fluctuations for different apparent gains. The circle markers correspond to traces shown in **b**. The full line represents a fit of the gain dependence. 43

7.1 (a) and (b) Simulated charge distributions in a Hall bar. A pixel represents 0.5 μm. (c) Frequency shifts of the mechanical resonance for the two distributions shown in (a) and (b) for the first 7×7 resonant modes. (d) and (e) Reconstructed charge distribution based on the frequency shifts in (c). 47
7.2 Scattering parameter of the probe tone as a function of pump frequency. Inset shows last measured mode. 48
7.3 Scattering parameter with probe tone at the fundamental mode $S_{21,0}$ as a function of pump tone frequency. The gray shaded area indicates the measurement range in Fig.7.2. Inset shows last measured mode. 49

CHAPTER 1

Introduction

Microelectromechanical systems (MEMS) integrate mechanical sensors and actuators at the microscale to other physical domains [32]. These miniature devices profited from semiconductor manufacturing techniques and quickly spread everywhere. If you pulled out your phone and the screen lit up or used parking assistance for your car, you used MEMS inertial devices [42]. If you used game controllers, RF or satellite communication, lab-on-a-chip or other drug delivery systems, you probably used MEMS as well [65]. The list of MEMS applications is extensive and growing fast. Most schemes are based on coupling static devices or mechanical oscillators to the parameter to be measured and detecting changes in the properties of the MEMS. The performance of a device is benchmarked by the responsitivity - the ratio of sensor output to input parameter - and the sensitivity - the minimum detectable change in the input parameter [87].

Silicon nitride membranes are a particular class of MEMS presenting world-record force sensitivities [45, 78, 97, 35, 49] and unimaginable quality factors of above 10 billion [9]. This thesis exploits the sensitivity of Silicon nitride membranes to study condensed matter physics interactions in everyday conditions: without high magnetic fields, special piezoelectric materials, or cavities. This ambitious project is only possible by developing a new platform inspired by two known techniques: mass spectroscopy with cantilevers and electrostatic detection with membranes. The first technique determines the mass of single proteins based on the frequency of out-of-plane vibrational modes in a cantilever. The cantilever behaves as a spring-mass system with resonance frequency inversely proportional to the square root of the oscillating mass. Once a molecule adsorbs to the surface of the cantilever, the frequency of the vibrational modes shifts and the total mass of the system is determined with atomic resolution and spatial distribution [26, 36, 37]. The second technique senses electrostatic force between two capacitor plates: a conductive membrane flipped on top of an electrode. The applied DC voltage between the two plates generates an electrostatic force [48, 99], which alters the effective spring constant of the membrane and, therefore, its frequency. The voltage between the electrode and the membrane is determined by the shift in the resonant frequency.

This thesis combines these two techniques in one extremely versatile platform: everyday electromechanics (EEM). The method capacitively couples a metallized silicon nitride membrane to a sample under scrutiny and is compatible with standard transport and reflectometry techniques [23, 60, 75, 4]. The applications are multifold, so here we present how to implement EEM and begin to explore a few of its applications in 8 chapters. Chapter 2 provides the theoretical background of the model to understand the device, based on the supplementary

information of the article Puglia et al. [76]. The simulations required to design the experiment considering DC and AC voltages, as well as, keeping the environment at room temperature or cooling it to liquid nitrogen temperatures are introduced in Chapter 3. Chapter 4 details the fabrication procedures of the flip-chip. The measurement setup and the measurements acquired in a high impedance environment and at low temperatures are presented in Chapter 5. The measurements in 50 Ω environment and room temperature were published in Puglia et al. [76] and shown in chapter 6. Here it is explored how everyday electromechanics can be used as a low-loss inductor, for parametric amplification or remote cooling of mechanical motion. Chapter 7 expands these measurements to higher order mechanical modes and introduces two-tone spectroscopy. A preliminary study indicates that characterizing higher-order modes provides spatial information about the electrode as well. A brief conclusion and outlook finalize the thesis in Chapter 8.

CHAPTER 2

Theoretical Background

This chapter aims to explain the theoretical model derived to explain the data and was published as supplement information in [76]. The extract follows bellow.

A simple way to understand capacitive coupling with EEM is to see it as a 1D problem of a mechanically compliant capacitor as shown in Fig. 1 of the main paper. It consists of a metallized silicon nitride membrane suspended over a stationary electrode with plate separation d. The 2D membrane maps on to this problem with some effective mass m, mechanical spring constant k_0, and capacitance C, which we cover later in Sec. 2.1. For the 1D problem, we consider a mechanical spring coupled to an electrical spring $H_{\rm int} = -\frac{1}{2}C(x)V_{\rm DC}^2$ where capacitance depends on the deflection of the spring and $V_{\rm DC}$ is applied DC bias. For the theoretical model, we consider that the applied $V_{\rm DC}$ is directly felt by the sample without the presence of a voltage shift ($V_{\rm DC} = V_{\rm DC,S}$). If we consider x to be the 1D coordinate of deflection of the mechanical spring from its equilibrium position in the absence of an applied DC bias, we can write a Hamiltonian for the system:

$$H = \frac{p^2}{2m} + \frac{1}{2}k_0x^2 + H_{\rm int}, \tag{2.1}$$

where p represents the momentum. From here forward, unless otherwise specified, we assume that C and its spatial derivatives C' and C'' are evaluated when x is at its mechanical equilibrium value $x = x_{\rm eqm}$. Expanding the capacitance about equilibrium gives

$$H_{\rm int} = -\frac{1}{2}C(x)V^2 \approx -\frac{1}{2}CV^2 - \frac{1}{2}C'V^2x - \frac{1}{4}C''V^2x^2. \tag{2.2}$$

The last term gives rise to an electrostatic spring constant, $k_e = -\frac{1}{2}C''V^2$, which is responsible for parametric electromechanical coupling. The second term indicates the presence of an electrostatic force, $1/2C'V^2$, which couples the mechanical resonator to propagating voltages. Considering a transmission line of impedance Z_i, the mechanical oscillator couples to the propagating voltages at a rate $g_i = C'^2V_{\rm DC}^2Z_i/m$ and to a dissipative bath at a rate $\kappa_{\rm in}$. The total mechanical linewidth is $\kappa_{\rm in} + g_1 + g_2 + ...$. Considering a standard line impedance of 50 Ω (Z_0) and $V_{\rm DC}$ below 30 V to facilitate integration to other circuit elements, it is necessary to carefully choose the geometry parameters to reach the strong coupling limit $g_i > \kappa_{\rm in}$. Below, we present a theoretical model for capacitive coupling with EEM and some of it's applications.

2.1 Continuum model

We start our endeavor by imagining a rectangular membrane with side lengths L_y, L_z and 2D density ρ_{2D}, under a pre-stress σ. It is described by a continuum Lagrangian density [53]

$$\mathcal{L} = \mathcal{T} - \mathcal{V} = \frac{1}{2}\rho_{\mathrm{2D}}\dot{u}^2 - \frac{1}{2}\sigma h|\nabla u|^2 - \mathcal{U}, \tag{2.3}$$

where h is the thickness of the membrane, $\mathcal{U} = -\frac{1}{2}\frac{\epsilon_0}{d+u}V^2$ is the electromechanical interaction energy, and $u(V, y, z, t)$ is the 2D continuum displacement from the zero-bias equilibrium position in the vertical direction, with ϵ_0 being the vacuum permittivity and V the total voltage.

2.1.1 Small dynamic displacement

We will allow for large static displacements plus a small dynamic part. Assuming that the dynamic part does not effect the static solution, justified only for small dynamics, we will independently solve the static problem and expand about this solution to find the dynamics. The static problem is solved in Sec. 2.1.2.

To expand around the static solution, we separate variables into static and dynamic parts $V(t) = V_{\mathrm{DC}} + V_{\mathrm{AC}}$, and $u(V, y, z, t) = u_0(V_{\mathrm{DC}}, y, z) + u_1(V_{\mathrm{AC}}, y, z, t)$. Expanding $\mathcal{U}$ up to quadratic order in dynamical variables and neglecting terms that couple u_0 and V_{AC} gives

$$\mathcal{U} \approx -\frac{\epsilon_0}{2(d+u_0)}V_{\mathrm{DC}}^2 + \frac{\epsilon_0}{2(d+u_0)^2}u_1(V_{\mathrm{DC}}^2 + 2V_{\mathrm{DC}}V_{\mathrm{AC}}) - \frac{\epsilon_0}{2(d+u_0)^3}u_1^2V_{\mathrm{DC}}^2. \tag{2.4}$$

Inserting this expansion into Eq. 2.3, the Lagrangian density breaks into static and dynamic parts $\mathcal{L} = \mathcal{L}_0 + \mathcal{L}_1(t)$. The static Lagrangian density $\mathcal{L}_0$ is identical to Eq. 2.6, which gives the static displacement. The dynamic Lagrangian density is

$$\mathcal{L}_1 = \frac{1}{2}\rho_{\mathrm{2D}}\dot{u_1}^2 - \frac{1}{2}\sigma h|\nabla u_1|^2 + \frac{\epsilon_0}{2(d+u_0)^3}u_1^2V_{\mathrm{DC}}^2 - \frac{\epsilon_0}{(d+u_0)^2}u_1V_{\mathrm{DC}}V_{\mathrm{AC}}. \tag{2.5}$$

To arrive at the expression for the static Lagrangian density, we cancel the cross term $\sigma h\nabla u_0 \cdot \nabla u_1$ arising from the expansion of the mechanical potential with the static $u_1V_{\mathrm{DC}}^2$ in Eq. 2.4 by making use of the equations of motion for u_0 (Eq. 2.7) and the boundary conditions of u_1. Physically, this is a consequence of the fact that static forces must balance in equilibrium.

2.1.2 Static solution

Starting from Eq. 2.3, we seek a static solution u_0 with $\dot{u}_0$=0. u_0 has the Lagrangian density $\mathcal{L}_0$

$$\mathcal{L}_0 = -\frac{1}{2}\sigma h|\nabla u_0|^2 + \frac{1}{2}\frac{\epsilon_0V_{\mathrm{DC}}^2}{d+u_0}. \tag{2.6}$$

The Euler-Lagrange equation gives the equilibrium condition for u_0,

$$\sigma h\nabla^2u_0 = \frac{\epsilon_0V_{\mathrm{DC}}^2}{2(d+u_0)^2}. \tag{2.7}$$

Expanding the above expression for $u_0 \ll d$ results in a linear equation of motion, which is solved in terms of the Fourier series $u_0(V,y,z) = \sum_{a,b} \ell_{ab}(V) f_{ab}(y,z)$ with $f_{ab}(y,z) = \sin(\frac{a\pi y}{L_y})\sin(\frac{b\pi z}{L_z})$. The Fourier coefficients ℓ_{ab} are

$$\ell_{ab}(V) = -\frac{8\epsilon_0 V_{\mathrm{DC}}^2 \Phi_{ab}/(d^2\pi^2 ab)}{\rho_{2D}\Omega_{0,ab}^2 - \frac{\epsilon_0 V_{\mathrm{DC}}^2}{d^3}}, \tag{2.8}$$

where $\Omega_{0,ab}$ is the zero voltage mechanical frequency for modes a, b, and $\Phi_{a,b}$ is the mode matching factor with $\Phi_{a,b} = \frac{ab\pi^2}{4L_yL_z}\iint_{\mathcal{S}} \sin(\frac{a\pi y}{L_y})\sin(\frac{b\pi z}{L_z})dydz$, where $\mathcal{S}$ is the electrode surface under the membrane. In case of perfect electrode-membrane overlap, $\Phi_{a,b} = 1$ for a, b odd and $\Phi_{a,b} = 0$ if a or b is even. The expression above reduces to $\ell_{ab} = \frac{2C'_{pp}V_{\mathrm{DC}}^2\Phi_{a,b}}{\pi^2 abm\Omega_{pp,ab}^2}$, with $\Omega_{pp,ab}^2 = \Omega_{0,ab}^2 - \Omega_{e,pp}^2$, $C'_{pp} = -\epsilon_0 L_y L_z/d^2$ and an electromechanical frequency shift in the parallel capacitor approximation $\Omega_{e,pp}^2 = \frac{\epsilon_0 V_{\mathrm{DC}}^2 L_y L_z}{4md^3}$.

2.1.3 Effective 1D model

To create an effective model, one may decompose the displacement into a sum of normal modes times an amplitude function $x_{n,j}(t)$,

$$u_{1,nj}(y,z,t) = x_{n,j}(t)\sin\left(\frac{n\pi y}{L_y}\right)\sin\left(\frac{j\pi z}{L_z}\right) \tag{2.9}$$

and insert into the linearized Lagrangian density. Due to the orthogonality of the normal modes, the Lagrangian $L_1 = \int dydz\mathcal{L}_1$ becomes a sum of independent contributions from each normal mode, $L_1 = \sum_{n,j} L_{1,n,j}$. Each normal mode is equivalent to a simple harmonic oscillator with position $x_{\mathrm{n,j}}$,

$$L_{1,n,j} = \frac{1}{2}m\dot{x}_{n,j}^2 - \frac{1}{2}m\Omega_{m,nj}^2 x_{n,j}^2 + C'V_{\mathrm{DC}}V_{\mathrm{AC}}x_{n,j}. \tag{2.10}$$

The effective mass is $m = \rho_{2\mathrm{D}}L_xL_y/4$. The resonance frequency is given by

$$\Omega_{m,nj}^2 = \Omega_{0,nj}^2 - \Omega_e^2 \tag{2.11}$$

where $\Omega_{0,nj}^2 = \frac{\sigma h}{\rho_{2\mathrm{D}}}\left(\frac{\pi^2 n^2}{L_y^2} + \frac{\pi^2 j^2}{L_z^2}\right)$ is the bare resonant frequency and $\Omega_e^2 = C''V_{\mathrm{DC}}^2/2m$ is the electromechanical frequency shift. The capacitance $C = \int \frac{\epsilon_0}{d+u_0}dydz$ and its derivatives

$$C' = -\int \frac{\epsilon_0 \sin\left(\frac{n\pi y}{L_y}\right)\sin\left(\frac{j\pi z}{L_z}\right)}{(d+u_0)^2}dydz, C'' = 2\int \frac{\epsilon_0 \sin^2\left(\frac{n\pi y}{L_y}\right)\sin^2\left(\frac{j\pi z}{L_z}\right)}{(d+u_0)^3}dydz \tag{2.12}$$

can be calculated numerically. Equation 2.10 defines a 1D model equivalent to the electromechanical spring model introduced in Eq. 2.1.

2.1.4 Large dynamic displacements

We derived an effective 1D model under the assumption of small dynamic displacements. This assumption can be relaxed by instead taking advantage of the fact that we have a high-Q system and making use of a rotating wave approximation. Instead of expanding the Lagrangian

in orders of $V_{\rm AC}$, u_1 and neglecting coupling between u_0 and $V_{\rm AC}$, we can instead collect terms in the Lagrangian oscillating at 0ω, ω, 2ω. The upshot is that there is now a static contribution from $\langle V_{\rm AC}^2\rangle$, where $\langle . \rangle$ denotes a time average. One can include this term by using the formulae in Sec. 2.1.3 with the substitution

$$V_{\rm DC}^2 \to V_{\rm DC}^2 + \langle V_{\rm AC}^2 \rangle. \tag{2.13}$$

2.2 Collapse physics

As shown in Eq. 2.11, the DC voltage causes corrections to the mechanical resonant frequency Ω_m according to $\Omega_m^2 = \Omega_0^2 - \Omega_e^2$. The equilibrium position $x_{\rm eq}$ also depends on voltage. The dependence can found exactly by minimizing the potential part of the energy, solving

$$x_{\rm eq} = \frac{C'(x_{\rm eq})V^2}{2m\Omega_m^2}. \tag{2.14}$$

Since C' depends on x, this gives a cumbersome expression. The important result is that for sufficiently strong voltages there are no longer stable minima. A parallel-plate capacitor with plate separation d then collapses once $x_{\rm eq}/d \approx 0.67$.

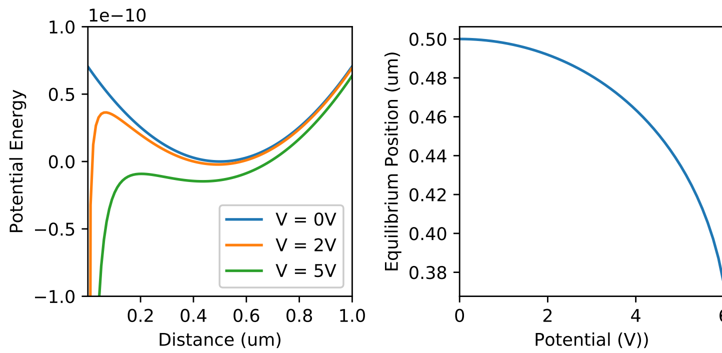

Figure 2.1: (a) potential energy by plate separation with a static applied voltage. Note that as a larger static bias is applied, the minimum becomes increasingly unstable. (b) equilibrium value of x by applied voltage.

A leading-order approximation can be found by neglecting the collapse physics. For a parallel plate one then finds

$$x_{\rm eq}(V) \approx \frac{-\epsilon_0 A V^2 \Phi_{n,j}}{2md^2\Omega_m^2}, \tag{2.15}$$

valid well below the collapse voltage.

2.3 Dynamics

We return to the dynamic Lagrange's equations for a single mode (Eq. 2.10) to write the equation of motion of x

$$m\ddot{x} = -m\Omega_m^2 x + C' V_{\rm DC} V_{\rm AC}, \tag{2.16}$$

where we have have dropped the n, j subscripts for convenience. We want to consider an applied voltage $V_{\rm AC} = |V_{\rm AC}| \cos\omega t$ and add a phenomenological damping parameter $\kappa_{\rm in}$ to

describe mechanical dissipation. With these changes, we obtain the linearized equation of motion

$$m\ddot{x} = -m\Omega_m^2 x - m\kappa_{\text{in}}\dot{x} + F_{\text{em}}, \tag{2.17}$$

where $F_{\text{em}} = C' V_{\text{DC}} |V_{\text{AC}}| \cos \omega t$ is the electrostatic force. We can also write (2.17) in the frequency domain as follows:

$$-\omega^2 x = -\Omega_m^2 x - i\omega\kappa_{\text{in}} x + F_{\text{em}}/m, \tag{2.18}$$

where we have divided by m for simplicity. This equation is solved in frequency space by

$$x = \chi_m F_{\text{em}}/m, \tag{2.19}$$

where $\chi_m = (\Omega_m^2 - \omega^2 + i\kappa_{\text{in}}\omega)^{-1}$ is the mechanical susceptibility and i is the imaginary unit. Note that since C' considers the mode matching factor, the force will be zero for even modes coupled to an electrode with full overlap. Note also that if $V_{\text{AC}} = |V_{\text{AC}}| cos(\omega_2 t)$ and $\omega_2 \gg \omega$, than the force component at ω is zero and therefore $x(\omega)$ is zero.

2.4 Coupling to a circuit

To understand coupling to an electrical circuit, one may start with the constitutive relation for a capacitor $q = CV$. Differentiating gives $I = \dot{C}V + C\dot{V}$. Given a varying current $I = I_0 + I_1 e^{i\omega t}$, we again keep only terms oscillating at ω, arriving at $I_1 = i\omega C' x V_{\text{DC}} + i\omega C V_{\text{AC}}$. Finally, inserting the solution for x gives

$$I_1 = (Z_m^{-1} + Z_C^{-1}) V_{\text{AC}}, \tag{2.20}$$

where the mechanical impedance is $Z_m^{-1} = i\omega C'^2 V_{\text{DC}}^2 \chi_m / m$. As pointed out in Ref. [94], one can now construct an effective circuit model consisting of the mechanical impedance in parallel with the capacitor impedance $Z_C^{-1} = i\omega C$. The membrane impedance is equivalent to that of a series RLC circuit with parameters

$$C_{\text{eff}} = \frac{C'^2 V_{\text{DC}}^2}{m\Omega_m^2} \tag{2.21}$$

$$L_{\text{eff}} = \frac{1}{\Omega_m^2 C_{\text{eff}}} \tag{2.22}$$

$$R_{\text{eff}} = \kappa_{\text{in}} L_{\text{eff}}. \tag{2.23}$$

This gives the expected circuit resonant frequency of Ω_m and linewidth κ_{in}. A key insight is that for typical silicon nitride membranes and moderate voltages, one can already obtain $R \sim 50\ \Omega$. Thus, the odd-index modes of the mechanical oscillator can be matched to the transmission line.

2.4.1 Antiresonance

The balancing of a gate capacitance by the RLC circuit gives rise to an antiresonance. The antiresonance occurs when the imaginary part of the total reactance Y is zero. Using $Y = Y_m + Y_C$ and $Y_m = i\omega g \chi_m / Z_0$ gives an approximate expression for the antiresonance frequency Ω_a

$$\Omega_a^2 = \Omega_m^2 + \frac{g}{Z_0 C}, \tag{2.24}$$

valid when the antiresonance is detuned from Ω_m by much more than a linewidth. When the linewidth is dominated by coupling, this condition is equivalent to $1/(\Omega_m C) \gg Z_0$, which is well satisfied even for the largest achievable capacitances.

For analysis of the antiresonance frequency, it is useful to express Ω_a in terms of the bare mechanical resonance and geometric quantities. Combining with the bias-dependence of resonance frequency (see Sec. 2.1.2) gives

$$\Omega_a^2 = \Omega_0^2 + \left(\frac{C'^2}{C} - \frac{C''}{2}\right)\frac{V_{\mathrm{DC}}^2}{m}, \tag{2.25}$$

where C, C', and C'' are determined numerically (Eq. 2.12).

2.4.2 Mechanical damping from a transmission line

A physical view of damping can be given by writing down a dressed mechanical susceptibility due to the electromechanical interaction. To do this, let's think about a minimal setup where the oscillator is coupled to a single port through a transmission line with impedance Z_0. An incoming wave generates a force proportional to V_{AC}^+. However, Eq. 2.17 considers an external driving force proportional to $V_{\mathrm{AC}} = V_{\mathrm{AC}}^+ + V_{\mathrm{AC}}^-$. This reflects the fact that a reflected wave will be generated by the mechanical oscillator, which also generates a force. As we will see below, the force from this reflected wave is responsible for damping.

To see how this comes about, we need to write the mechanical susceptibility to the applied force, which is proportional to V_{AC}^+. Differentiating $q = CV$ and inserting the expression for current $I = (V_{\mathrm{AC}}^+ - V_{\mathrm{AC}}^-)/Z_0 = (2V_{\mathrm{AC}}^+ - V_{\mathrm{AC}})/Z_0$ we find the expression

$$V = 2V_{\mathrm{AC}}^+ - i\omega C' Z_0 x V_{\mathrm{DC}}, \tag{2.26}$$

where we have neglected the effect of the gate capacitance for simplicity.

Inserting this result into the frequency-domain version of Eq. 2.17 we find

$$-\omega^2 x = -\Omega_m^2 x - i\omega\left(\kappa_{\mathrm{in}} + \frac{Z_0(C'V_{\mathrm{DC}})^2}{m}\right)x + 2C'V_{\mathrm{DC}}V_{\mathrm{AC}}^+/m. \tag{2.27}$$

We can immediately see that the susceptibility to an incident wave $\overline{\chi}_m = (\Omega_m^2 - \omega^2 + i\kappa_{\mathrm{eff}}\omega)^{-1}$ is dressed with an effective damping rate

$$\kappa_{\mathrm{eff}} = \kappa_{\mathrm{in}} + g, \tag{2.28}$$

where $g = \frac{Z_0(C'V_{\mathrm{DC}})^2}{m}$ is the electromechanical coupling. We can then write the mechanical displacement on the incoming signal,

$$x = 2\sqrt{\frac{g}{m}}\overline{\chi}_m \frac{V_{\mathrm{AC}}^+}{\sqrt{Z_0}}. \tag{2.29}$$

2.4.3 Scattering parameters from Z

Now that we have a model for the impedance seen by the transmission line, $Z^{-1} = Z_m^{-1} + Z_C^{-1}$, scattering parameters can be written down for the three possible configurations of the transmission line: with a single port, with two identical ports, and with two different ports.

To treat different line impedances symmetrically, its useful to work with power waves, defined for instance by

$$v_1^+ = V_1^+/\sqrt{Z_0}, \tag{2.30}$$

where $V_{\rm i}^+$ is the incident wave on port i. Note that $|v_1^+(t)|^2$ then has units of power and $|v_1^+(f)|^2$ has units of energy spectral density. This also makes them nice to work with from the perspective of thermodynamics.

1 port

In a one-port reflection configuration one has $S_{11} = (Z - Z_0)/(Z + Z_0)$ where Z_0 is the characteristic impedance of the transmission line. A simple limit for understanding the results is to work near resonance and neglect the gate impedance, taking $Z \approx Z_m$. One then finds

$$\begin{aligned} S_{11} &\approx 1 - \frac{2Z_0}{Z_0 + Z_m} && (2.31)\\ &= 1 - 2ig\omega\overline{\chi}_m. && (2.32) \end{aligned}$$

The same expression can also be found by neglecting gate capacitance in Eq. 2.20, which gives $v^- = v^+ - i\omega\sqrt{gm}x$, and then combining with Eq. 2.29.

What is the temperature of the mechanical oscillator? In the limit that the dominant coupling is to the transmission line (g large) the position spectral density $S_{\rm xx}$ is related to the electrical power spectral density of v_1^+, $S_{+,+}$ by

$$S_{\rm xx} = 4\frac{g}{m}|\overline{\chi}_m|^2 S_{+,+}. \tag{2.33}$$

Using $\int_0^\infty |\overline{\chi}_m|^2 = 1/(\kappa\Omega_m^2)$, and equipartition $k_B T_m = m\Omega_m^2\langle x^2\rangle$ we find, $k_B T_m = S_{+,+}$, where k_B is the Boltzmann constant. If port 1 is in equilibrium then Johnson-Nyquist noise gives $S_{+,+} = k_B T_+$, so

$$T_m = T_+, \tag{2.34}$$

confirming that the mechanics equilibrates with the transmission line when it is strongly coupled.

2 port

In a 2-port transmission configuration $S_{21} = 2Z_0/(2Z_0 + Z)$. For general transmission-line impedances on ports one (Z_1) and two (Z_2), the transmission is $2Z_2/(Z_1 + Z_2 + Z)\cdot\sqrt{Z_1/Z_2}$, where the last factor is present because we work with power waves. One can see that when $R_{eff} \ll Z_2$ one approaches unity transmission on resonance. Thus, the mechanical oscillator acts as a low-insertion loss bandpass filter. The reflection coefficient from port 1 is $S_{11} = 1 - 2Z_1/(Z_1 + Z_2 + Z)$.

One can then proceed in analogy with Sec. 2.4.3 to find scattering parameters. For instance, one finds

$$\begin{aligned} S_{21} &= 2i\omega\sqrt{g_1 g_2}\overline{\chi}_m && (2.35)\\ S_{11} &= 1 - 2i\omega g_1\overline{\chi}_m. && (2.36) \end{aligned}$$

where now

$$\kappa_{\rm eff} = \kappa_{\rm in} + g_1 + g_2, \tag{2.37}$$

and the coupling constants are $g_i = C'^2 V_{\rm DC}^2 Z_i/m$ for a port with input impedance Z_i.

To understand the effect on the mechanics we write

$$I = \frac{1 - S_{11}}{Z_1} V_1^+ + \frac{S_{12}}{Z_1} V_2^+, \tag{2.38}$$

where V_2 is the incident voltage wave on port 2. In analogy with Sec. 2.4.3 find

$$x = \overline{\chi}_m \left(\sqrt{\frac{g_1}{m}} v_1^+ + \sqrt{\frac{g_2}{m}} v_2^+ \right) \tag{2.39}$$

We can now determine which port the mechanical oscillator thermalizes to in the strong-coupling limit that $g_1 + g_2 \gg \kappa_{\rm in}$. In the limit of equal line impedances $g_1 = g_2$ and thermal fluctuations enter in equally from the two ports. In the more general case

$$S_{\rm xx} = \frac{|\overline{\chi}_m|^2}{m} \left(g_1 S_{1+,1+} + g_2 S_{2+,2+} \right). \tag{2.40}$$

We see that the mechanical oscillator will thermalize to a weighted sum of the temperatures from the two ports.

2.4.4 Dissipation and resonant transmission

Dissipation associated with $\kappa_{\rm in}$ can be easily incorporated by adding a third virtual port with impedance Z_3 given by

$$Z_3 = \frac{m\kappa_{\rm in}}{C'^2 V_{\rm DC}^2}. \tag{2.41}$$

To understand the consequences, consider a model with one physical port and with mechanical dissipation coupled through a virtual port v. Imagine for simplicity that the physical port is at zero temperature. The voltage fluctuations measured at port 1 are then only those originating from the virtual port, satisfying $v_1^- = S_{13} v_3^+$, where we can read off the transmission coefficient from the two-port model. The fluctuations at port 1 then satisfy

$$S_{1-,1-} = 4 g_1 \kappa_{\rm in} \omega^2 |\overline{\chi}_m|^2 k_B T. \tag{2.42}$$

The thermo-mechanical noise transmitted on resonance is then

$$S_{1-,1-} = \frac{4 g_1 \kappa_{\rm in}}{(g_1 + \kappa_{\rm in})^2} k_B T. \tag{2.43}$$

We see that thermo-mechanical noise is resonantly transmitted when the impedance matching condition $g_1 = \kappa_{\rm in}$ is satisfied.

2.4.5 Input-output theory

In analogy with cavity optomechanics, these findings can be neatly summarized by an input-output theory. This will give the same results as the impedance formalism, but is more convenient. The fundamental input-output relation derived from $q = CV$ and neglecting gate capacitances is

$$v_i^- = v_i^+ - i\omega \sqrt{g_i m} x. \tag{2.44}$$

This must be combined with the equations of motion for x,

$$x = 2\sqrt{\frac{g_i}{m}} \overline{\chi}_m v_i^+, \tag{2.45}$$

where as before $\overline{\chi}_m$ is the damped linewidth, and the sum over i is implied by the repeated index. Scattering parameters $S_{ij} = \langle v_i / v_j \rangle$ and power spectra can be immediately derived from the above equations.

2.5 Parametric gain

Mechanical parametric amplification was first studied in Ref. [82]. Later work studied gain in the presence of a cavity and generalized to non-zero detunings in Ref. [12].

Imagine the case where a voltage is applied at twice the mechanical frequency. Due to the electromechanical spring effect, this introduces a parametric shift in the mechanical frequency $\Omega_0^2 h_0 \sin(2\Omega_m t)$ where $h_0 = 2V_{2\Omega_m}/V_{\mathrm{DC}}$. According to Ref. [82] we should expect mechanical gain in a single quadrature. The equation of motion of the membrane becomes:

$$\ddot{x} + \kappa_{\mathrm{in}}\dot{x} + \Omega_m^2 x(1 + h_0 \sin(2\Omega_m t)) = F/m. \tag{2.46}$$

To solve, we introduce quadrature components x_I and x_Q,

$$x = x_I(t)\cos(\Omega_m t) + x_Q(t)\sin(\Omega_m t), \tag{2.47}$$

which can be encoded by quadrature vectors $\vec{x} = (x_I, x_Q)$, with a similar decomposition for F. Keeping only terms varying at Ω_m, the equations of motion become

$$\ddot{\vec{x}} + \kappa_{\mathrm{in}}\dot{\vec{x}} + 2\Omega_m i\boldsymbol{\sigma_y}\dot{\vec{x}} + \kappa_{\mathrm{in}}\Omega_m i\boldsymbol{\sigma}_y\vec{x} + \frac{\Omega_m^2 h_0}{2}\boldsymbol{\sigma}_x\vec{x} = \frac{1}{m}\vec{F}, \tag{2.48}$$

where $\boldsymbol{\sigma}_x$ and $\boldsymbol{\sigma}_y$ are Pauli matrices in quadrature space. Changing into frequency domain, we can collect terms

$$(-\omega^2 + i\kappa_{\mathrm{in}}\omega)\vec{x} + \Omega_m(\kappa_{\mathrm{in}} + 2i\omega)i\boldsymbol{\sigma}_y\vec{x} + \frac{\Omega_m^2 h_0}{2}\boldsymbol{\sigma}_x\vec{x} = \frac{1}{m}\vec{F}, \tag{2.49}$$

or explicitly as a $2x2$ matrix equation

$$\begin{pmatrix} -\omega^2 + i\kappa_{\mathrm{in}}\omega & \frac{\Omega_m^2 h_0}{2} + \Omega_m\kappa_{\mathrm{in}} + 2i\Omega_m\omega \\ \frac{\Omega_m^2 h_0}{2} - \Omega_m\kappa_{\mathrm{in}} - 2i\Omega_m\omega & -\omega^2 + i\kappa_{\mathrm{in}}\omega \end{pmatrix} \begin{pmatrix} x_I \\ x_Q \end{pmatrix} = \frac{1}{m}\begin{pmatrix} F_I \\ F_Q \end{pmatrix}. \tag{2.50}$$

This matrix is easily invertible to solve for x_I and x_Q. This gives quadrature susceptibilities

$$\begin{pmatrix} x_I \\ x_Q \end{pmatrix} = \begin{pmatrix} \chi_0 & \chi_{12} \\ \chi_{21} & \chi_0 \end{pmatrix}\begin{pmatrix} F_I/m \\ F_Q/m \end{pmatrix} \tag{2.51}$$

with

$$\chi_0 = \frac{i\omega(\kappa_{\mathrm{in}} + i\omega)}{(\kappa_{\mathrm{in}} + 2i\omega)^2\Omega_m^2 - (\kappa_{\mathrm{in}} + i\omega)^2\omega^2 - h_0^2\Omega_m^4/4} \tag{2.52}$$

$$\chi_{12} = \frac{-\Omega_m\kappa_{\mathrm{in}} - 2i\omega\Omega_m - \Omega_m^2 h_0/2}{(\kappa_{\mathrm{in}} + 2i\omega)^2\Omega_m^2 - (\kappa_{\mathrm{in}} + i\omega)^2\omega^2 - h_0^2\Omega_m^4/4} \tag{2.53}$$

$$\chi_{21} = \frac{\Omega_m\kappa_{\mathrm{in}} + 2i\omega\Omega_m - \Omega_m^2 h_0/2}{(\kappa_{\mathrm{in}} + 2i\omega)^2\Omega_m^2 - (\kappa_{\mathrm{in}} + i\omega)^2\omega^2 - h_0^2\Omega_m^4/4} \tag{2.54}$$

On resonance ($\omega = 0$) $\chi_0 = 0$, and it is small for all frequencies in the high-Q limit. The gains are $G_{ij} = \chi_{ij}(h_0 \neq 0)/\chi_{ij}(h_0 = 0)$, with zero-frequency ($\omega = 0$) values

$$G_{12}^0 = G_A = \frac{\kappa_{\mathrm{in}}}{\kappa_{\mathrm{in}} - \Omega_m h_0/2}, \; G_{21}^0 = G_S = \frac{\kappa_{\mathrm{in}}}{\kappa_{\mathrm{in}} + \Omega_m h_0/2}. \tag{2.55}$$

The solution for $x_{Q/I}(\omega)$ can be approximated by a Lorentzian with a height $G_{A/S}$ and a bandwidth $\kappa_{\text{in}}/G_{A/S}$,

$$\begin{pmatrix} x_I \\ x_Q \end{pmatrix} \approx \frac{1}{\kappa_{\text{in}}\Omega_m} \begin{pmatrix} 0 & \frac{i\kappa_{\text{in}}/2}{\omega - i\kappa_{\text{in}}/(2G_A)} \\ \frac{-i\kappa_{\text{in}}/2}{\omega - i\kappa_{\text{in}}/(2G_S)} & 0 \end{pmatrix} \begin{pmatrix} F_I/m \\ F_Q/m \end{pmatrix} = \frac{1}{m}\boldsymbol{\chi}_m \vec{F}, \tag{2.56}$$

where the last equality defines the matrix susceptibility $\boldsymbol{\chi}_m$.

We can redefine the equation of motion in terms of a gain function ($\boldsymbol{G}$) and an undriven susceptibility $\boldsymbol{\chi}_m^0$:

$$\vec{x} = \frac{1}{m}\boldsymbol{G}\boldsymbol{\chi}_m^0 \vec{F} \tag{2.57}$$

with

$$\boldsymbol{G} = \begin{pmatrix} \frac{\omega - \frac{i\kappa_{\text{in}}}{2}}{\omega - i\kappa_{\text{in}}/(2G_A)} & 0 \\ 0 & \frac{\omega - \frac{i\kappa_{\text{in}}}{2}}{\omega - i\kappa_{\text{in}}/(2G_S)} \end{pmatrix} \tag{2.58}$$

$$\boldsymbol{\chi}_m^0 = \frac{1}{\kappa_{\text{in}}\Omega_m} \begin{pmatrix} 0 & \frac{i\kappa_{\text{in}}/2}{\omega - i\kappa_{\text{in}}/2} \\ \frac{-i\kappa_{\text{in}}/2}{\omega - i\kappa_{\text{in}}/2} & 0 \end{pmatrix} \tag{2.59}$$

2.5.1 Quadrature input-output theory

Since the parametric gain problem was solved in terms of quadratures, we need a quadrature input-output theory in analogy to Sec. 2.4.5. From the derivative rule $\dot{x} \to \Omega_m \boldsymbol{\sigma}_y \vec{x} + \dot{\vec{x}}$, we find the relation analogous to Eq. 2.44,

$$\vec{v}_j^- = \vec{v}_j^+ - i\sqrt{g_j m}(\Omega_m \boldsymbol{\sigma}_y + \omega)\vec{x}. \tag{2.60}$$

We now need to write the quadrature equations of motion in terms of an input wave $\vec{v}^+$, in analogy with Eq. 2.45. Writing $\vec{F}$ in terms of the total voltage and eliminating the out-going wave $\vec{v}^-$ using Eq. 2.60 gives

$$\frac{\vec{F}}{m} = 2\sqrt{\frac{g_j}{m}}\vec{v}_j^+ - ig_j(\Omega_m \boldsymbol{\sigma}_y + \omega)\vec{x}, \tag{2.61}$$

where for multiple ports one must simply sum the right side over j. The first term on the right-hand side is the force due to the incoming wave. The second term can by identified, after substitution into Eq. 2.49, as introducing an effective damping at rate g_j. The linearized of motion can now be written down

$$\vec{x} = 2\sqrt{\frac{g_j}{m}}\overline{\boldsymbol{\chi}}_m \vec{v}^+, \tag{2.62}$$

where the dressed susceptibility $\overline{\boldsymbol{\chi}}_m$ is the same as $\boldsymbol{\chi}_m$ but with an effective linewidth $\kappa_{\text{eff}} = \kappa_{\text{in}} + g_j$. Additional ports can be added by introducing more summands into the above equation.

These input-output relations make it straightforward to calculate scattering parameters and power spectral densities in the presence of gain. To get tidy expressions, we can neglect the ω in Eq. 2.60, valid when the position quadratures are slowly varying ($\omega \ll \Omega_m$), which gives the scattering formula

$$\vec{v}_j^- = (1 + \boldsymbol{\chi}_{jj}^{\text{lin}})\vec{v}_j^+ + \boldsymbol{\chi}_{jk}^{\text{lin}}\vec{v}_k^+ + \dots, \tag{2.63}$$

where the linearized susceptibility is

$$\boldsymbol{\chi}_{jk}^{\text{lin}} = -2i\sqrt{g_j g_k}\Omega_m \boldsymbol{\sigma}_y \boldsymbol{\chi}_m = \begin{pmatrix} \frac{i\sqrt{g_j g_k}}{\omega - i\kappa_{\text{eff}}/(2G_S)} & 0 \\ 0 & \frac{i\sqrt{g_j g_k}}{\omega - i\kappa_{\text{eff}}/(2G_A)} \end{pmatrix} \tag{2.64}$$

and the ... denote analogous terms for more ports. We finally see that that the output modes consists of a prompt-reflected input mode, plus each mode squeezed in phase and amplified out of phase. This expression is reminiscent of Eq. 2.36. In fact, when there is no gain ($h_0 = 0$, $G_A = G_S = 1$), we have $\boldsymbol{\chi}_m = \frac{-1}{\kappa_{\text{in}}\Omega_m}\frac{\kappa_{\text{in}}/2}{\omega - i\kappa_{\text{in}}/2}\boldsymbol{\sigma}_y$, and we arrive at a linearized version of Eq. 2.36.

Power spectra are also straightforward at the level of Eq. 2.63 because all matrices are diagonal; there are no cross-correlations between quadratures.

2.5.2 Position inference

From the previous section, in particular Eq. 2.63, it's trivial to write the outgoing power spectral density S_{--} in terms of the incoming ones S_{++}. It's less trivial to relate S_{--} to the position spectral density S_{xx}. This is trickier because $\vec{v}_j^{\,+}$ and $\vec{x}$ are correlated. We need to work with a power spectral matrix $BW\vec{v}_j^{\,-} \otimes \vec{v}_j^{\,*-}$, where BW is the measurement bandwidth and $\otimes$ is the outer product. Assuming the input field is in a thermal state, $\vec{v}_i^{\,+} \otimes \vec{v}_j^{\,*+} = k_B T\delta_{ij}$, we find the power spectral matrix

$$\boldsymbol{S}_{--} = (1 + 2\text{Re}[\boldsymbol{\chi}_{11}^{\text{lin}}])k_B T + gm\Omega_m^2 \boldsymbol{S}_{\text{xx}}, \tag{2.65}$$

where $\text{Re}[x]$ denotes the real part of x and we have labeled the measurement port as $j = 1$. As a check, one can verify that without gain and with only one input field, the above expression is equal to $k_B T$, which is expected because our quadrature definition gives $\langle x^2\rangle = \langle x_I^2\rangle/2 + \langle x_Q^2\rangle/2$.

Undriven Position Fluctuations

We can now combine equations (2.57) and (2.62) to write the position fluctuations in terms of an undriven susceptibility and the incoming scattering waves at port i:

$$\boldsymbol{S}_{xx,i} = 4\frac{g_i}{m}|\boldsymbol{G}|^2|\overline{\boldsymbol{\chi}}_m^0|^2 \boldsymbol{S}_{i+i+}. \tag{2.66}$$

The total undriven position fluctuations ($\boldsymbol{S}_{xx} = |\boldsymbol{G}|^2\boldsymbol{S}_{xx}^0$) is the sum of the fluctuation contributions from each port i:

$$\boldsymbol{S}_{xx}^0 = \frac{4}{m}|\overline{\boldsymbol{\chi}}_m^0|^2 \sum_i g_i \boldsymbol{S}_{i+i+} = \frac{1}{m\Omega_m^2}\frac{\kappa}{\omega^2 + (\kappa/2)^2}\sum_i \frac{g_i}{\kappa}\boldsymbol{S}_{i+i+}. \tag{2.67}$$

We can define the undriven bath temperature (T_m) as the average of the incoming radiation, weighted by the coupling:

$$k_B T_m = \sum_i \frac{g_i}{\kappa}\boldsymbol{S}_{i+i+}. \tag{2.68}$$

On resonance the expression for the bath temperature reduces to $m\Omega_m^2\boldsymbol{S}_{xx} = 4k_B T_m$. In the high gain limit, the outgoing power spectral density can be approximated from the position fluctuations:

$$\boldsymbol{S}_{--} = gm\Omega_m^2|\boldsymbol{G}|^2\boldsymbol{S}_{xx}^0. \tag{2.69}$$

Area analysis

In the experiment, we can estimate the mechanical temperature by analyzing the area of Lorentzians in power spectral density traces. A handy relation is

$$\int \frac{1}{(2\pi f)^2 + (\frac{\kappa}{2G})^2} df = \frac{G}{\kappa}. \tag{2.70}$$

The area associated with the Lorentzian parts of Eq. 2.65 evaluates to

$$A = g\left(m\Omega_m^2 \langle x_I^2 \rangle - k_B T\right). \tag{2.71}$$

In thermal equilibrium we get $A = 0$, as required for equilibrium white noise.

Imagine a situation where the input mode has a known temperature T, but the mechanics is coupled to additional ports that, in the absence of gain, would set it to some temperature T_m. T_m can be understood as the temperature of the mechanical bath. Using Eq. 2.62 and carrying out the frequency integral for the amplified quadrature gives the area

$$A = gk_B(G_A T_m - T). \tag{2.72}$$

In our experiment we measure the output mode v_o from a coupler, which can be accounted for with the additional input-output relation

$$\vec{v}_o = \sqrt{\eta}\vec{v}^- + \vec{v}_{\text{add}}, \tag{2.73}$$

where v_{add} accounts both for added thermal noise due to loss the added noise of the chain. Here η includes both the directional coupler and system losses between the sample and the measurement device. The output area A_o is a factor of η smaller than the input area A, so we have

$$\frac{A_o}{k_B g} = \eta G_{\text{A}} T_m - \eta T. \tag{2.74}$$

For simplicity, we can redefine the area as $A_{\text{eq}} = A_o/g$ and gain as $G_{\text{eq}} = \eta G_A$. In addition, we need to relate the apparent gain measured in the experiment to G_A. The apparent gain is measured using the increase in the height of a pilot tone, as shown in the following section.

2.5.3 Signal recovery and apparent gain

Imagine there is one physical port with coupling g_1 and a dissipation port with coupling κ_{in}. For the amplified quadrature, the output noise on resonance is

$$S_{\text{mm}} = \eta\left(1 - G_A \frac{2g_1}{\kappa_{\text{in}} + g_1}\right)^2 S_{++} + \eta\left(G_A \frac{2\sqrt{\kappa_{\text{in}} g_1}}{\kappa_{\text{in}} + g_1}\right)^2 S_{00} + S_{\text{add}} \tag{2.75}$$

When measuring, we referred to an apparent gain $G_{\text{app}}^0 = \sqrt{\eta}|1 - 2G_A \frac{g_1}{\kappa_{\text{in}} + g_1}|$. Inverting this expression gives G_A in terms of the apparent gain,

$$G_A = \frac{\kappa_{\text{in}} + g_1}{2g_1}\left(\frac{G_{\text{app}}}{\sqrt{\eta}} + 1\right), \tag{2.76}$$

which should be used in the area analysis discussed in Sec. 2.5.2.

The input-referred noise of the amplified quadrature is

$$S_{++} + \frac{\kappa_{\rm in} g_1}{\omega^2 + (g_1 - \kappa/(2G_A))^2} S_{00} + \frac{1}{G_{\rm app}^2} S_{\rm add}, \tag{2.77}$$

where we have introduced the frequency-dependent apparent gain $G_{\rm app}^2(\omega) = |1 + \chi_m^{\rm lin}|^2$, which satisfies $G_{\rm app}(0) = G_{\rm app}^0$. The second term in Eq. 2.77 represents the unavoidable addition of noise due to mechanical loss, and the third term is the noise added by the subsequent components, which is suppressed by gain.

For a 2-port device, i.e., a device with two physical ports and a virtual one, an analogous derivation can be done. Consider we add an incoming wave $\vec{v}_1^{*+}$ to port 1 while measuring the outgoing wave from port 2 and that the only incoming radiation at port 2 comes from its thermal fluctuations. For the amplified quadrature, the output noise on resonance is

$$S_{\rm mm} = \eta \left(1 - G_A \frac{2g}{\kappa_{\rm eff}}\right)^2 S_{2+2+} + \eta \left(G_A \frac{2g}{\kappa_{\rm eff}}\right)^2 S_{1+1+} + \eta \left(G_A \frac{2\sqrt{\kappa_{\rm in} g}}{\kappa_{\rm eff}}\right)^2 S_{00} + S_{\rm add}. \tag{2.78}$$

where $\kappa_{\rm eff} = \kappa_{\rm in} + 2g$. We can once again relate the apparent gain to G_A

$$G_A = \frac{\kappa_{\rm eff}}{2g} \frac{G_{\rm app}}{\sqrt{\eta}}. \tag{2.79}$$

2.6 Converting 2-port measurement into 1-port measurement

A two-port measurement is limited by the room-temperature noise contribution of multiple ports. We would like to convert to a one-port measurement in order to minimize the noise added by ports. Naively, one could take this measurement as shown in Fig. 2.2(a), using a power splitter to add the reflected and transmitted portions of the signal together. However, returning to (2.35) and (2.36) shows that when $g_1 = g_2$, $S_{21} + S_{11} = 1$. No information is gained from this measurement.

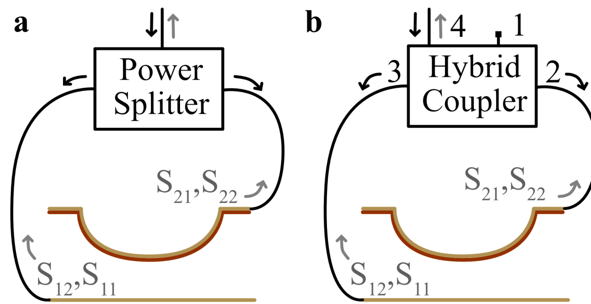

Figure 2.2: Two possible configurations for a one-port measurement. (a) Using a power splitter to add reflected and transmitted components. (b) Using a hybrid coupler to subtract reflected and transmitted components.

Another possible approach, as shown in Fig. 2.2(b), is to use a hybrid coupler, which adds a $180°$ phase shift to one port, in place of a power splitter. The scattering matrix of a hybrid coupler is:

$$[S] = \frac{-i}{\sqrt{2}} \begin{bmatrix} 0 & 1 & 1 & 0 \\ 1 & 0 & 0 & -1 \\ 1 & 0 & 0 & 1 \\ 0 & -1 & 1 & 0 \end{bmatrix}. \tag{2.80}$$

A signal a incident on port 4 of the hybrid coupler (the Δ port) will generate a signal of $-ia/\sqrt{2}$ out of port 3 and a signal of $ia/\sqrt{2}$ out of port 2, both of which will interact with the sample. We can assume reciprocity, $S_{21} = S_{12}$, and symmetry, $S_{11} = S_{22}$, which gives a signal of

$$\frac{ia}{\sqrt{2}}(S_{21} - S_{11}) \tag{2.81}$$

incident on port 3. Likewise, port 2 receives a signal of

$$\frac{ia}{\sqrt{2}}(S_{11} - S_{21}). \tag{2.82}$$

The hybrid coupler again modifies the signal from ports 3 and 2 by $-i/\sqrt{2}$ and $i/\sqrt{2}$, respectively, and combines them, returning a signal of

$$a(S_{21} - S_{11}). \tag{2.83}$$

Returning again to (2.35) and (2.36), we evaluate the ratio of the returned signal to the original signal for $g_1 = g_2$:

$$S_{out} = (1 - 4i\omega g\bar{\chi}_m), \tag{2.84}$$

giving us a device which is effectively converted to a one-port configuration.

2.6.1 Conservation of energy in converted measurement

Equation (2.84) can be evaluated on resonance to:

$$S_{out} = 1 - \frac{4i\omega g}{i(\kappa_{\text{in}} + 2g)\omega} \tag{2.85}$$

for $\kappa = \kappa_{\text{in}} + 2g$ according to (2.37). In the case of zero loss ($\kappa_{\text{in}} = 0$) this works out to

$$S_{out} = 1 - \frac{4g}{2g} = -1 \tag{2.86}$$

which corresponds to a sign change in voltage but no power loss. This is the same as (2.36) for $g \to 2g$.

2.7 Noise Temperature

We have developed a protocol to determine the added noise temperature of the EEM amplifier based on a two-point temperature calibration. The noise temperature for individual voltage trace (V_{-}) is calculated as described in 2.5.2 with G_{app}

$$G_{\mathrm{app}} = \frac{V_{-}}{P_t/ATT}, \tag{2.87}$$

where the attenuation (ATT) is the ratio of measured voltage fluctuations due to a probe tone and its amplitude (P_t). The input referred noise of the membrane amplifier $T_{\mathrm{ref}}(G_{\mathrm{m}})$ is calculated by T_m/G_{eq} and measured for a reference resistor at RT (295 K) and LN (70 K) temperature. The intercept value of $T_{\mathrm{ref}}(G_A)$ gives the added noise temperature (T_{add}) of the membrane amplifier.

CHAPTER 3

Design Simulation

This chapter aims to explain the studies performed to simulate the static and dynamical deflection of the membrane, the design the layout of the chip, and the optmization of radiowave transmission through the bottom electrode.

3.1 Dynamic deflection of the Membrane

Mode shape simulations were done using the eingenfrequency solver of Comsol Multiphysics version 5.6. Comsol divides the structure into a fine mesh and uses finite element analysis to solve partial differential equations at each node of the mesh. The membrane was simulated by creating a layered material and assigning one layer as high stress Si_3N_4 and another as gold without pre-stress. The gold layer adds mass and relaxes the pre-stress of the Si_3N_4 (σ_{SN}) to an effective metallized stress σ [53]

$$\sigma = \frac{t_{\mathrm{SN}}}{t_{\mathrm{SN}} + t_{\mathrm{gold}}} \sigma_{\mathrm{SN}}, \tag{3.1}$$

with $t_{\mathrm{SN}}/t_{\mathrm{gold}}$ being the thickness of the Si_3N_4 membrane/gold layer. Both the added mass and stress relaxation decrease the mechanical resonance frequency. The mode shape itself does not change with the metallization and, as Eq.2.9 suggests, the mode shape for square membranes are sine-like. In order to break the degeneracy of (a,b) and (b,a) modes, the membrane was made rectangular, with one side being 2 μm bigger than the other. Unfortunately it was not possible to apply DC voltage to the layered material to check the distortion of the mode shapes caused by capacitive forces. Therefore, the mode shapes presented here are the solution of the dynamic deflection suffered my the membrane under an AC voltage. The static deflection of the membrane was solved with Mathematica and presented in Sec. 3.2.

Figure 3.1(a-d) presents the dynamic mode shape for 4 modes: (1,1), (2,1), (2,2), and (3,1) at 0 DC voltage. The mode shape of the mode (1,2) looks like its pair (2,1), but rotate by 90°. It is also known that degenerate modes hybridize, creating a non-sine like mode [96, 71, 22, 84]. This was the case for modes (4,2) and (2,4) simulated with Comsol, which became the hybrid mode shapes shown in Fig. 3.1(e-f). The hybrid modes can be obtained by summing the sine like version of mode (2,4) (Fig. 3.1(g)) and its 90° rotated pair. In particular, the sum 1:1 of the sine like modes return the mode shape in Fig. 3.1(h) and reproduces the hybrid mode simualted by Comsol. In order to verify if the modes hybridize, the simulation would have to be cross-checked by a measurement technique, as for example, optical interferometry.

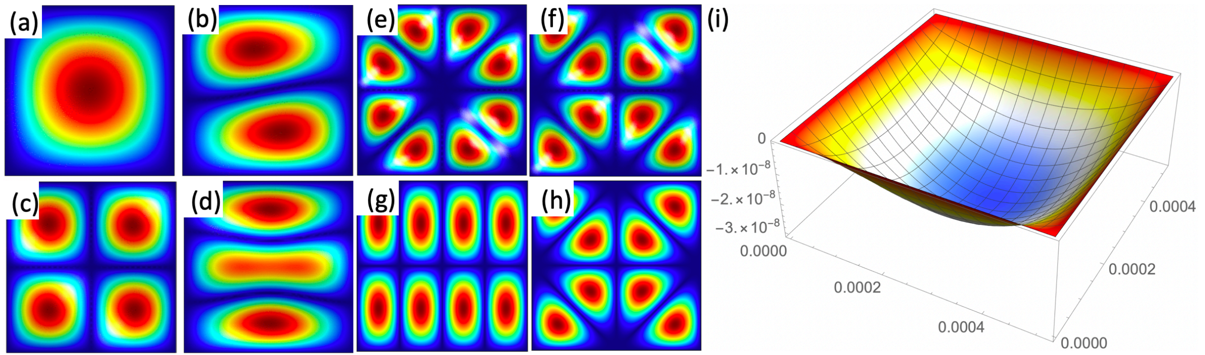

Figure 3.1: (a-d) Comsol simulation of the mode shape from a square membrane for modes (1,1), (2,1), (2,2), and (3,1). (e-f) Hybrid modes simulated by comsol at the eigenfrequencies from modes (4,2) and (2,4). (g) Sine-like mode (2,4) (h) Sum 1:1 of the sine-like modes (2,4) and (4,2) (i) Static deflection of a 500 μm membrane under $V_{\rm DC} = 1$ as calculated with Mathematica.

3.2 Static deflection of the membrane

The deflection of the membrane under DC voltage is described by the partial differential equation 2.7. This equation was solved numerically using the function NDSolveValue in Mathematica and considering Dirichlet Boundary Conditions, i.e., the deflection along the edges is zero. For the full code, please refer to Appendix I. Figure 3.1(i) shows the solution for a 521 μm membrane and $V_{\rm DC} = 1$. Contrary to the dynamic deflection, the static deflection is not well described by a single sine-like mode shape, but rather a sum of them (see Sec.2.1.2). This results in a deflection shape that is flatter at the bottom, than the fundamental mode shown in Fig. 3.1(a). The amplitude of the static deflection is orders of magnitude higher than the dynamic deflection, which only reaches a maximum deflection of around 30 nm.

3.3 Flip-Chip design

The flip-chip design was simulated with Comsol Multiphysics version 5.2a. The height of the posts on the bottom chip determines the separation distance when the bottom posts touch the top ones. This assertion assumes that there is no undesired particles between the two chips and that both top and bottom chips are flat. The front etch eases the cleanliness requirement, but the flatness requirement is not met if the epoxy (stycast 2850FT catalyst 23LV) used to fix the top and bottom chips expands or contracts in comparison to the silicon. Stycast was applied at room temperature and once the flip-chip is cooled, stycats will shrink about 15 times more than the silicon, due to its higher thermal expansion coefficient. The chip will therefore bend, changing the separation distance betweem the membrane and the electrode. The bowing in the center of the chip can be minimized by carefully placing the outer posts.

Figure 3.2 (a) simulates the displacement perpendicular to the membrane plane for top and bottom chip glued by stycast at RT and then cooled to liquid nitrogen temperatures. Given the 90°-symmetry of the problem, it is possible to set two perpendicular planes with symmetry boundary conditions, reducing the geometry to one quarter of the chip. Even though the membrane chip bends around the edges at low temperature, the center displacement remains approximately 150 nm by placing the posts 300 nm from the chip edge.

To further minimize the risk of center displacement, later designs include inner posts that rest

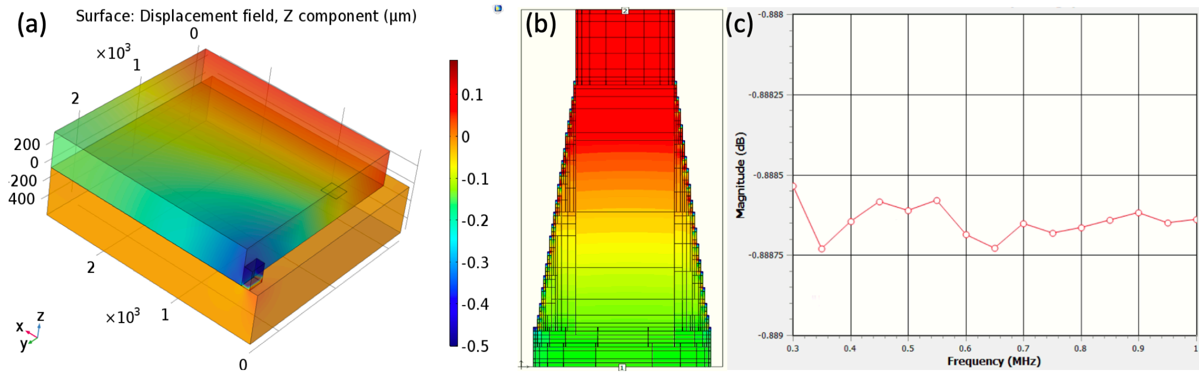

Figure 3.2: (a) Comsol simulation of the bending of the top chip due to the cooling to liquid nitrogen temperatures. The center of the chip is located at the left edge, while the stycast is placed on the bottom edge. (b) Electrode geometry considered for the simulation of scattering parameter S_{21} along the electrode. (c) Scattering parameter S_{21} along the electrode simulated with Sonnet. Such electrode would be flipped under a 500 μm membrane.

on the frame around the membrane (see Fig.4xi). These inner posts do not make a difference if the membrane chip bows up, but help preventing the membrane chip from bowing down. It is useful to point out that hurdling the deformation with the inner posts creates stress on the top chip, which might cause unwanted effects on the membrane. Furthermore, the inner posts help to prevent the collapse of the membrane due to downwards bowing, but play no role on the collapse due to applied voltage.

3.4 Sonet Simulations

Electromagnetic simulations with the software Sonet version 17.52.1 were carried out to estimate the transmission of electromagnetic waves within the electrode. Figure 3.2 (b) shows the geometry considered for a 50 nm thick platinum electrode under a 500 μm square membrane. We considered a conductivity of 9.43 MS/m and de-embedding for the electromagnetic simulation. Figure 3.2 (c) shows the transmission of electromagnetic waves between two ports located at the extremes of the electrodes. The frequency range focus around the mechanical frequency of a 500 μm square membrane at 0 DC voltage (380 kHz) and at around 10 % of the collapse voltage (330 kHz). There is a negligible 0.89 dB loss betweem the extremes of the elctrodes, i.e., the bottom, where the electrode is bonded to a PCB, and the top, where the membrane is flipped.

CHAPTER 4

Fabrication Techniques

An EEM die was produced by first fabricating the bottom and top chip and then flipping the membrane die on top of the electrode. This chapter focus on explaining the fabrication techniques used in this process.

4.1 Flip-Chip Fabrication

Figure 4.1 i-vi shows the fabrication procedure of the membranes. The procedure is as follows:

i. 50 nm of high-stress Si_3N_4 is deposited through Low Pressure Chemical Vapor Deposition (LPCVD) on a high-resistivity silicon wafer. The wafer is bought ready from the company Hahn-Schickard.

ii. Both sides of the wafer are covered with resist. A window is opened on the resist covering the back side of the wafer using photolithography. This window defines the size of the Si_3N_4 membrane.

iii. The exposed Si_3N_4 is removed with reactive-ion etching (RIE) and the remaining Si_3N_4 acts as a mask to protect silicon from being etched. The leftover resist is stripped.

iv. Steps 2 and 3 are repeated on the front side of the wafer, removing Si_3N_4 from everywhere except around the posts and the membrane. The front etch reduces the requirement of cleaningness of the chip, as small particles ($< 30\mu m$) will no longer push the bottom and top chips apart.

v. The back side of the wafer is exposed to KOH, etching the silicon from the exposed window and releasing the membrane. The front part of the wafer is then exposed, creating the posts.

vi. The membrane is cleaned to remove etch residues and then metallized by evaporating gold at 25° angle on the back side of the wafer using ebeam evaporation. At the end, the wafer is diced.

The bottom electrodes are fabricated as shown in figure 4.1 vii-xi:

vii. a high/resistivity silicon wafer is used a substrate.

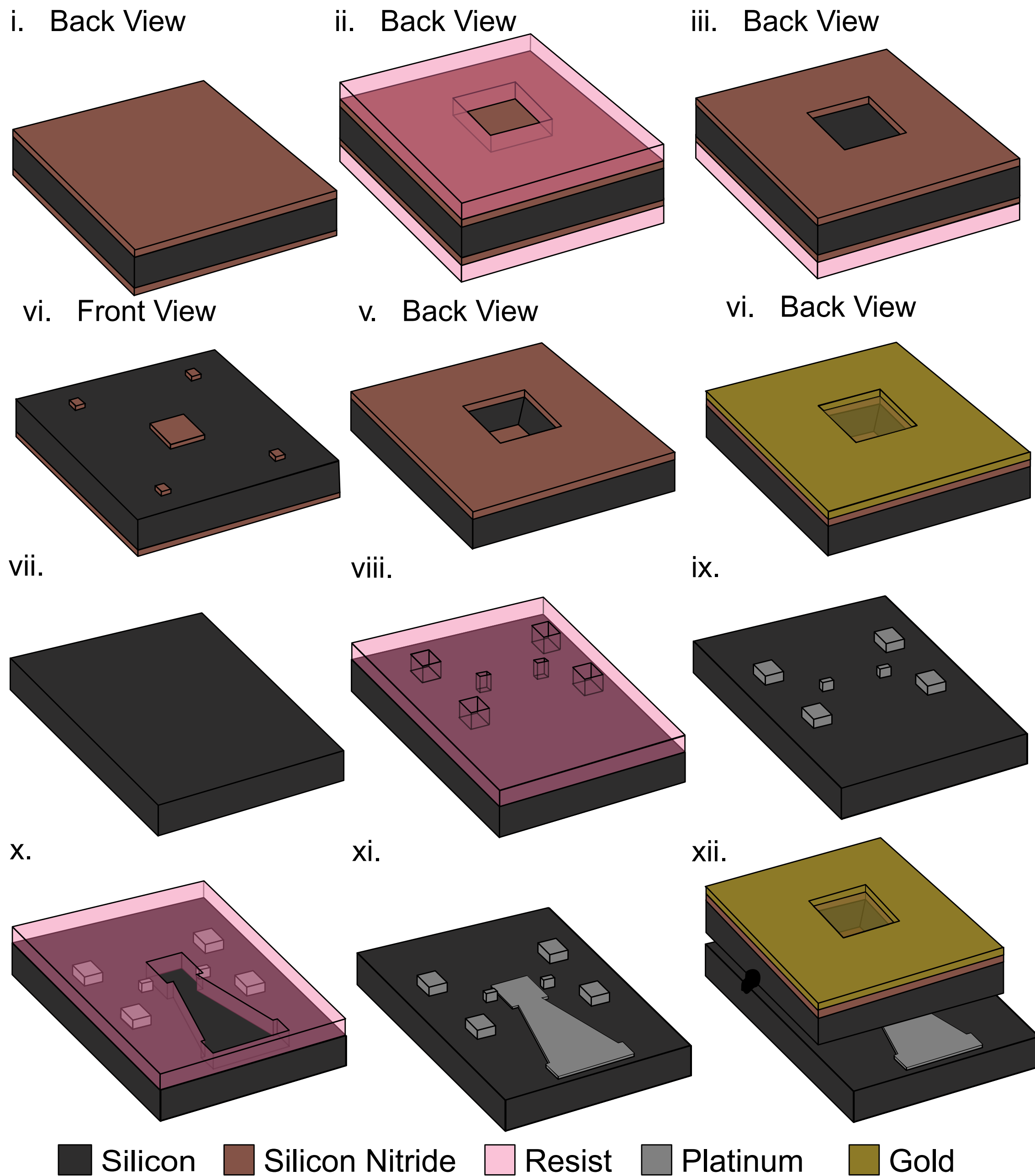

Figure 4.1: Fabrication process of a flip-chip. Membrane Fabrication: (i) high-resistivity silicon is covered in Si_3N_4, (ii) photolithography exposes a window which defines the membrane size, (iii) Si_3N_4 is etched with RIE, (iv) photolithography and RIE are used to remove Si_3N_4 from the front side, defining the area of the posts and the membrane, (v) KOH etches the silicon, and (vi) the membrane is metallized with gold. Electrode Fabrication: (vii) high-resistivity silicon is used as substrate, (viii) photolitography exposes the regions for the posts, (ix) posts are evaporated, (x) a second photolithography exposes the region for the electrode, (xi) the electrode is evaporated, and the wafer is dices and cleaned. (xii) The membrane chip is flipped on top of the electrode.

viii. Photolitography exposes the substrate, where the posts will be evaporated.

ix. 350 nm of platinum are evaporated at 0.1 nm/s rate using e-beam evaporation and the resist is stripped.

x. A second photolithography defines the electrode shape.

xi. 50 nm of platinum is evaporated at 0.1 nm/s rate. The difference between the top of this layer and the top of the posts defines the separation distance between the top and the bottom chip (in this case 300 nm). The resist is stripped and a new layer of resist is spun on the front side of the wafer. Both sides of the wafer are covered in tape and the wafer is diced. The dice are individually cleaned in acetone, IPA and plasma etched.

Once both chips are fabricated we flip the membrane on top of the electrode using a die bonder. The chips are aligned and glued with stycast, see the representation in figure 4.1 xii. The chips are then ready to be bonded and measured.

4.2 Fabrication Techniques

This section focus on explaining the fabrication techniques used in this thesis.

4.2.1 Photolithography

This technique imprints a pattern onto a substrate by exposing a resist and then developping it. For the top chip, we first spin AZ6612 at 4000 rpm for 60 seconds and then baked at 125 ^{o}C for 50 seconds. The resist was exposed using a photomask aligner Suss Microtec MA6 in hard contact mode for 35 s. Development was done using MBQA. After evaporation the resist was stripped using acetone with sonication, and later rinsed in acetone and IPA.

For the bottom chip, we first spin LOR 5B for 60 seconds at 8000 rpm for the electrodes (1000 rpm for the posts). The chip was baked for 5 minutes at 170 ^{o}C and S1818 was spun for 30 seconds at 4000 rpm and baked for 1 minute at 115 ^{o}C. The resist was exposed with a dose of 150 mJ/cm^2 using the Photomask aligner EVG 610 and later developped in MF-319 for 40 seconds and then DI water for 1-2 minutes. Liftoff was done with acetone overnight or at 50 ^{o}C for 30 minutes. Finally the wafer was rinsed and sonicated in acetone and IPA.

4.2.2 Reactive Ion Etch

This technique combines the directionality of dry etching techniques with the high etching rates of wet etches by accelerating reactive ions towards the substrate. A reactive ion etch STS 320PC employed a mixture of CF_4 with flow rate 30 sccm and O_2 with flow rate 3 sccm to etch the equivalent of 52.5 nm of Si_3N_4. The process was carried using 150 W of RF power for 90 seconds.

4.2.3 Silicon Etch

KOH at 80 degrees was used as a silicon etchant, etching primarily the $<100>$ silicon plane at a 54.7° angle with the $<111>$ plane. Despite the high anisotropy of the etch rates with respect to silicon planes, it is not recommended to expose the wafer to KOH longer than necessary. The backside etch runs trough the whole 350 μm thick silicon, while the frontside

only removes 30 μm of silicon. Therefore a special holder was used to expose only the back side of the wafer for around 7 hours. At this stage, there are still 30 μm left of silicon on the backside. The wafer is, however, very fragile and it is not possible to turn it and fixate it to the holder for the front etch. Therefore, both sides of the wafer are exposed to the etchant, removing approximately 30 μm of silicon from both sides. Etching on both sides is a very energetic process and creates residues that were not observed in one-sided etch. These residues were later rinsed as described in section 4.2.4. After the etch, the wafer is rinsed thoroughly in water and dried by a perpendicular flow of N_2.

4.2.4 Membrane cleaning

Iron oxide residues were removed by dipping the wafer in HCl 37% for 6 minutes. The wafer was then rinsed in DI water two times. This procedure also removes the gold coating from the membranes, so it is important to perform it before the metalization.

4.2.5 E-beam Evaporation

This technique evaporates a target material by bombarding it with an electron beam. The bombardment vaporizes the target material which precipitates on the substrate. If parts of the sample are covered with resist, the resist is later lifted off while the metal directly in contact with the substrate stays.

E-beam evaporation was used to evaporate 50 nm (350 nm) of platinum for the electrodes (posts) using 3 nm of titanium as a sticking layer. The evaporation rate of metals for this thickness range muss be chosen carefully. High evaporation rates create in-plane stress in the evaporated layers, which is released in the form of Hillock grains, shown in Fig.4.2 (a). If present on the electrodes, these grains puncture through the membrane, if present on the posts, they increase the separation distance. Figure 4.2 (b) shows a smooth metal layer without Hillock grains obtained by evaporating platinum at a 0.1 nm/s rate.

The backside of the membrane was metallized with 25 nm of gold using 3 nm of titanium as a sticking layer. The metal layer has to be continuos across 3 regions: 1. the backside of the die, 2. the 54.7° step between region 1 an the etched silicon, 3. the membrane. At 0° evaporation angle (substrate parallel to evaporating material), the gold layer is not continuous between regions 1 and 2. By placing the electrode at an evaporation angle of 25°, a continuos metal layer is observed with 4 Ω resistance between region 1 and 3 as shown in figure 4.2 (c). Figure 4.2 (d) shows how the resistance across the step between regions 1 and 2 change as a function of evaporation angle. At angles higher than 25°, the metal creates a brim between regions 1 and 2 (see the inset from figure 4.2 (d)) and the resistance across these regions increases again.

Ebeam evaporation was also used the metallize the back side of the membrane wafer. The whole wafer is coated by a 3 nm titanium sticking layer, followed by 25 nm gold. Given the small thickness of this gold layer, no Hillock grains were observed. The wafer is then cleaved along small trenches that surround each die, so they are ready to be flipped.

4.2.6 Die Bonder

A die bonder model FNS 53XXBDA is used to flip the membrane chip on top of the electrode chip. The membrane is placed facing down on a teflon holder on top of a Thor Labs platform.

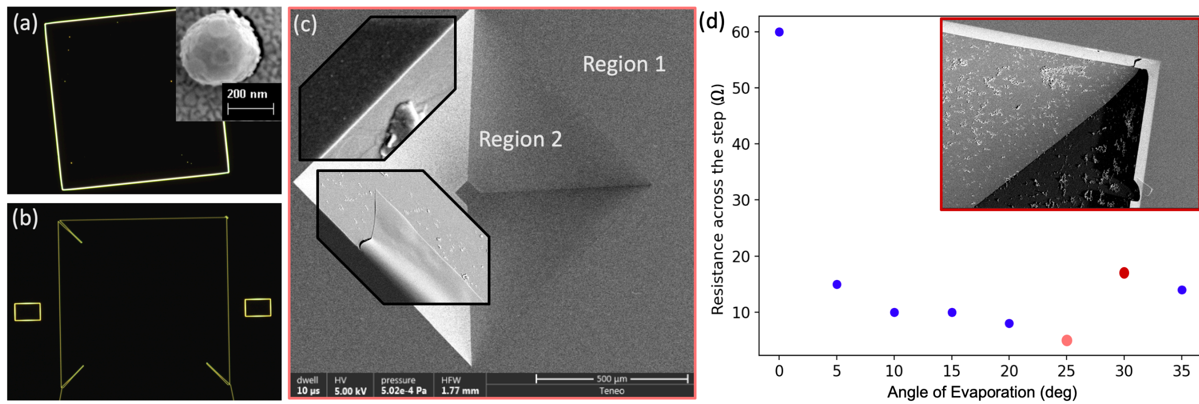

Figure 4.2: E-beam evaporation. (a) Dark field optical images of platinum on the electrode at 0.2 nm/s evaporation rate with the formation of Hillock grains (shown in the inset) and (b) at 0.1 nm/s without Hillock grains. (c) SEM of gold on the membrane at 25 deg evaporation angle. (d) Resistance across the step between region 1 and 2 as a function of evaporation angle. The inset shows the metal along the step for an evaporation angle of 30 deg.

Here it is important that only the edges of the chip touch the holder and the membrane remains pristine. A vacuum head picks up the membrane chip at a single point close to the edge of the membrane and brings it a few micrometers above the electrode. This way the chip can be pressed flat down against the bottom posts. The two chips are aligned and the Thor lab stage is raised until the posts on both chips touch. We then apply stycast 2850FT catalyst 23LV to the sides of the chips with an eyelash and wait for 15 minutes until the stycast starts to cure. After this stage, the separation distance between the top and bottom part is basicaly fixed. After another 24 hours, the stycast finishes curing and the chip is ready for bonding.

Figure 4.3 (a) shows a top view of a flip-chip. The golden backside of the membrane chip and the etched step are seen on the edges of the picture. An electrode with a 3/4 shape is seen through the membrane in the center of the picture. The silicon substrate, that usually appears dark gray, is seen in orange and the platinum in yellow. The change in color occurs due to the interference of light reflecting between the substrate and the membrane and indicates the separation distance betweem the two surfaces. Figure 4.3 (b) gives an estimation of the separation distance based on the color of the surfaces.

For higher separation distances (d $>$ 600 nm), the interference fringes are no longer visible and a filmetrics light interferometer F20 was used. The tool is designed to determine thickness of thin films. In this case, the air layer between the membrane and the electrode is the thin film we are trying to measure. Figure 4.3 (c) shows a filmetrics measurement and the model calculation for a separation distance of 3.3 μm. The wavelengths lower than 500 nm are absorbed by the Si_3N_4 membrane and an oscillation in the reflection intensity of higher wavelenths is caused by light interference inside the air layer. The calculation of the light reflection is based on a complex stack: 25 nm gold, 3 nm titanium, 50 nm Si_3N_4, air layer with unknown thickness, 50 nm platinum, 3 nm titanium, and a silicon substrate. Fixing all thicknesses but the air layer, we obtained the separation distance for the sample. These quick separation distance measurements would help us to acesss if the chip is worth bonding and measuring.

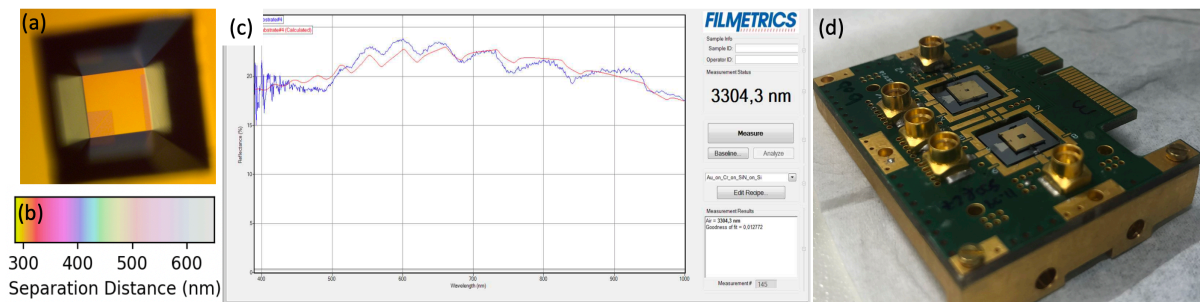

Figure 4.3: (a) Top view of a flip-chip taken with an optical microscope. A quarter electrode is seen as yellow in the middle while the silicon substrate appears in pink. (b) Separation distance infered from the interference between the membrane and the electrode. (c) Filmetrics reflectance meaurement in blue and fit for the thickness of the air layer in red. (d) PCB with two flip-chips ready to be loaded into the measuring chamber.

4.2.7 Wire Bonder

Wire bonding was carried out using a bonder model FNS 5330. The bonding force and time were chosen as the minimum possible. Bonds to the membrane chip were placed closed to stycast, minimizing the chance of collapsing the membrane. Figure 4.3 (d) shows a picture of two samples mounted and bonded to a printed circuit board. Note that the platinum here appears in light gray and the silicon in dark gray.

4.2.8 Uncollapsing Technique

A very important, if not the most important technique presented in this chapter, is how to uncollapse a membrane. During the electrical measurements, a spike or static voltage might add to V_{DC} overcoming the collapse threshold voltage. Membranes with 300 μm or less might be uncollapsed by pressing at the corners with a tweezer. The separation distance then is approximately restored and the membrane might present a static voltage, which appears as a DC voltage shift in the electrical measurements. Larger membranes ($>$500 μm) usually require more pressing on the corners to uncollapse and, unfortunately, the silicon frame of the membrane usually breaks before then.

CHAPTER 5

Measurement setup and non-everyday results

This chapter aims to explain the setup used for electrical measurements. More detailed results on low impedance S-Paramenter measurements and parametric amplification are presented in Chapter 6.

5.1 S-Parameters

Scattering parameters are a useful metric to characterize the propagation of electromagnetic waves in electrical networks. For a two port network, the scattering parameters are defined as

$$S_{11} = \frac{\mathrm{out}_1}{\mathrm{in}_1}\bigg|_{\mathrm{in}_2=0}, S_{12} = \frac{\mathrm{out}_1}{\mathrm{in}_2}\bigg|_{\mathrm{in}_1=0}, S_{21} = \frac{\mathrm{out}_2}{\mathrm{in}_1}\bigg|_{\mathrm{in}_2=0}, S_{22} = \frac{\mathrm{out}_2}{\mathrm{in}_2}\bigg|_{\mathrm{in}_1=0}, \tag{5.1}$$

where in/out is the incoming/outgoing radiation. For a matched circuit, all radiation is transmitted ($S_{21} = 1$) and nothing is reflected ($S_{11} = 0$). If, however, the circuit is mismatched, transmission will be lossy ($S_{21} < 1$). From Eq.2.21, it is clear that the EEM circuit is approximately 50 Ω matched on mechanical resonances, but mismatched at other frequencies. Therefore, measuring the scattering parameters allows us to characterize the mechanical resonator.

5.1.1 Measurement Setup

There are several ways of measuring the scattering parameter. In this thesis, we studied two: a reflection or effective single-port method and a two-port or transmission method. Figure 5.1(a) presents the transmission method. A microwave is sent from a lock-in amplifier through the coupled port of a directional coupler. A bias-tee adds DC voltage to the AC signal that arrives at the metallized membrane (port 1). The radio frequency is transmitted to the bottom electrode (port 2), where a DC ground is added through a bias-tee. The signal is then measured using a lock-in amplifier.

Figure 5.1(b) presents the magnitude of scattering parameter $|S_{21}|$ measured in transmission mode. A lorentzian peak is seen centered at the mechanical resonant frequency. On resonance, the electrical circuit is approximately 50 Ω matched, showing a transmission loss of less than

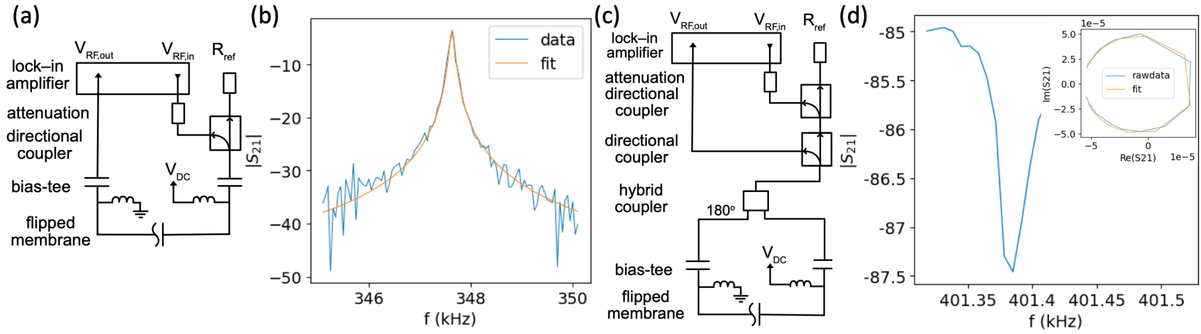

Figure 5.1: (a) Circuit diagram in transmission mode. (b) Scattering parameter S_{21} measured in transmission mode with a Lorentian fit. (c) Circuit diagram in reflection mode. (d) Scattering parameter S_{11} measured in reflection mode and an inset showing the imaginary and real components of S_{11}. A circular fit to these components allows us to obtain the circuit parameters.

4 dB. Out of resonance, the transmission decreases within a few Herz to the background transmission of around -50 dB. The transmission peak is fitted to Lorentzian curve (Eq.2.69), from which we extract the full-width half maximum (κ), the height of the lorentzian, and the mechanical frequency (Ω_m). This method is specially convenient for measuring low-loss circuits: as most of the signal is transmitted, a peak tens of dB tall is observed.

Figure 5.1(c) introduces the reflection method. An 180-degrees hybrid coupler is added between the bias-tees and the rest of the measurement chain. This hybrid coupler combines the reflected and transmitted signals, transforming the 2-port measurement into an effective 1-port measurement (see Sec.2.6). The reflected wave is then measured through the couple port of a directional coupler, completing the characterization of the scattering coeffiecient S_{11}.

Figure 5.1(d) presents the magnitude of scattering parameter $|S_{11}|$ measured in reflection mode and the inset presents the real and imaginary components of S_{11}. The magnitude of $|S_{11}|$ shows a dip at the mechanical resonant frequency. It is important to point out that the measurements shown in figures 5.1(b) and (d) are for different samples and have thefore different mechanical resonant frequencies. Note also that the signal is overcoupled and attenuated due to the directional coupler, so the dip in magnitude is only a few dB. A circular fit for the real and imaginary components of S_{11} allows us to obtain the full-width half maximum (κ), the external coupling (g), and the mechanical frequency (Ω_m).

5.1.2 High/Low Impedance Environment

The scattering parameters can be measured in a high or a 50 Ω impedance environment. The choice of input impedance depends on the application, with 50 Ω being the obvious choice for narrow band applications or when a low impedance network is required. High input impedance offers, however, around 0 dB of insertion loss, tunable linewidth up to kHz, and remarkable gain stabilities (see Sec. 5.2.2).

5.2 Parametric amplification

Section 2.5 introduces the theory of parametric amplifification. A pump tone was created by an arbitrary waveguide generator and added to the circuit through the coupled port of a directional coupler. The pump tone was locked to be exactly twice the frequency of a probe

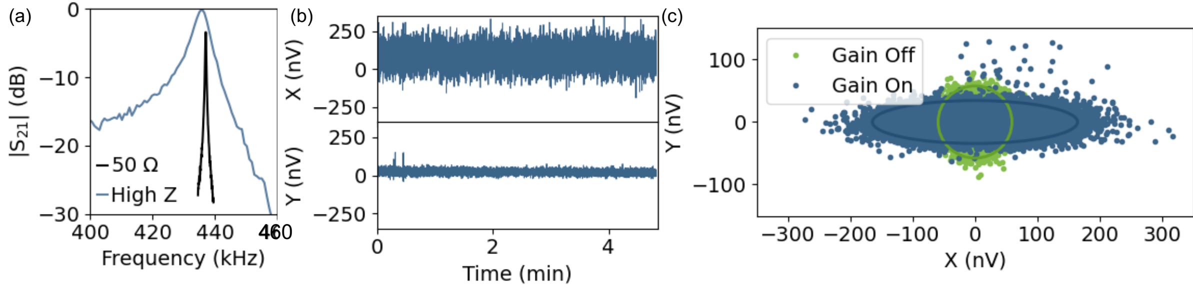

Figure 5.2: (a) Scattering parameter S_{21} measured in transmission mode for the measuring device being at high input impedance and at 50 Ω. (b) Demodulated X and Y time traces taken at high input impedance. (c) Demodulated X and Y quadratures with gain on and off taken at high input impedance. The solid line indicates $5\times$ the variance of the data.

tone, which was kept close to the mechanical frequency based on successive S_{21} measurements. The mechanical amplification causes the amplification of one voltage quadrature and their phase with respect to the measurement apparatus changes as the amplified wave travels down the circuit. Once at the measurment input port, the amplified radiation is measured and projected onto the X and Y quadratures of the demodulator.

5.2.1 Calibration

A phase and amplitude calibration converts the demodulated voltage into an amplified (X) and deamplified (Y) quadrature with gain G_A and G_S. The phase calibration is done by calculating the angle between the principal component of the demodulated voltage and the X-quadrature. By subtracting this phase from the demodulator's phase, the principal component rotates bringing the amplified quadrature to the X-axis.

The amplitude calibration is carried out by measuring the attenuation in the measurement chain based on a known tone. The conversion between apparent gain and G_A/G_S is explained in Sec. 2.5.3.

5.2.2 Results

Figure 5.2(a) shows a comparison of the magnitude of the scattering parameter S_{21} measured in transmission mode at 1.15 V for the high Z input impedance and 50 Ω option. As the resonance frequency depends primarily on V_{DC}, both resonances occur at approximately the same frequency. The 1.5 kHz difference between the two peaks can be explained by the constant slow red shift observed in the first hours pf pumping the vacuum chamber. The transmission on resonance is lossless at high input impedance, but about -4 dB for 50 Ω input impedance. The high input impedance Lorentzian shows a linewidth bigger than 4 kHz, while the 50 Ω input impedance Lorentzian has a linewidth of 0.3 kHz. This indicates the presence of extra damping at high input impedance. In this section, we will focus on further analysis of measurements taken with high input impedance.

Figure 5.2(b) presents the demodulated X- and Y-quadratures in high impedance mode under parametric amplification. The standard deviation of the X-quadrature is more than 5 times the Y-quadrature, confirming the amplification of the X-quadrature. The pump tone shifts the average of both quadratures away from zero, with a $5\times$ higher shift of the amplified

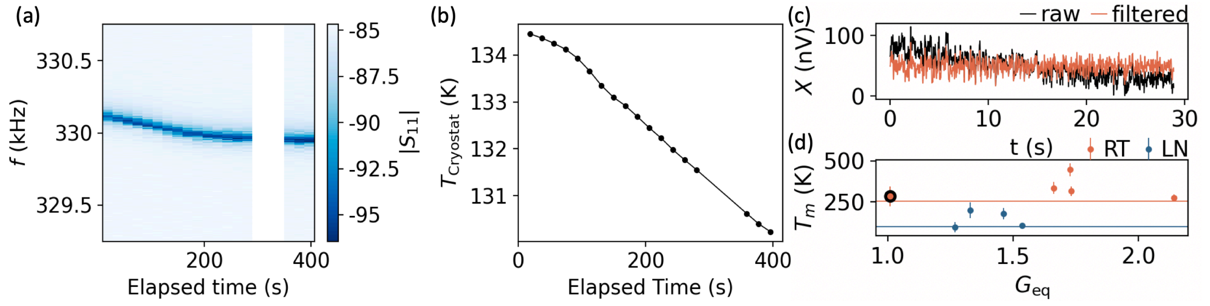

Figure 5.3: (a) Scattering parameter S_{11} as a function of frequency and ellapsed time. (b) Cryostat temperature as a function of time. (c) Voltage trace as a function of time for the amplified quadrature. (d) Mechanical Temperature with cryostat at LN temperature and a reference resistor at LN or RT. The black marker indicates the trace shown in (c).

quadrature. The trace is remarkably stable over 5 minutes, a feature that is not so common for similar traces taken with 50 Ω input impedance.

Figure 5.2(c) shows the demodulated quadratures with and without gain and 5$\times$ their standard deviation marked by an ellipsis. The 'gain off' data indicates that the noise is equally devided among the two quadratures, as expected. The "gain on" data shows the amplification of the X-quadrature by the shadowing of the unamplified trace and strech of the ellipsis parallel to the x-axis. Analogously, the squeezing of the Y-quadrature is noticed by the visibility of the underlying unamplified trace and the compression of the ellipsis along the y-axis. The amplification/squeezing is determined by the gain G_A/G_S introduced in Eq. 2.55.

5.2.3 Low temperature

This sections is dedicated to explain the experiments acquired by cooling the flip-chip to liquid nitrogen temperatures. Cooling the sample to LN temperatures decreases the internal dissipation κ_{in}, as the dissipative current gets frozen at low temperatures. The ratio of external coupling g/κ, therefore, increases from around 0.65 at RT to 0.85, bringing the device deeper into the strong coupling regime.

However, the slow 0.1 Hz/s shift in the mechanical resonant frequency at room temperature increases to 2 Hz/s at LN temperatures. This shift is explained by the higher adsorption of molecules on the surface of the membrane, which increases the mass of the resonator and lowers its frequency. There are three ways of diminishing the effects of this frequency shift on the measurements. The first is by switching the measurment to a high input impedance. Although the frequency shift rate does not change, the large linewidth of the mechanical resonance might provide enough stability for the intended measurement.

The second method stabilizes the resonant frequency by applying constant cooling. Cooling the membrane decreases its size due to thermal contraction, increasing the resonator frequency (see Eq. 2.11). The increase in the resonantor's mass is balanced by the decrease of its size and the frequency remains approximately constant, as shown in Fig. 5.3a. The cooling rate was increased to 10 mK/s at 100 seconds of ellapsed time (Fig. 5.3b), reducing the frequency shift to 0.2 Hz/s. A subsequent measurement was done after 350 s of elapsed time to track the the resonant frequency at later times. The stability obtained with this technique surpasses the requirement for our experiment, although a better frequency stability can be obtained with a heater controller that offers finer steps in cooling rate.

The third way of circumscribing the effects of the frequency shift is by acquiring short voltage traces and correcting the frequency shift by post-processing the data. Figure 5.3c shows a 30 seconds trace of a sample at LN temperature in 50 Ohm environment. The average voltage fluctuation decays from 80 nV to 20 nV within 30 seconds. This roll-off is corrected by applying a low-pass filter with time constant 0.7 s and a filtered trace is obtained by divinding the raw data by the roll-off fluctuations. A voltage spectral densities is then calculated and a lorentzian on top of a background is fitted to the data. The unamplified mechanical temperature T_m is proportional to the height of the lorentzian (Eq 2.68). Figure 5.3d shows T_m obtained with the reference resistor at RT or LN temperature, presenting an average of 331±61 K for RT meaurement and 146±45 K for the LN measurement. Both values are higher, but not far from the expected T_m of 254 K and 101 K for the reference resistor at RT and LN, respectively.

PID locking the measurement frequency to the resonance would in theory provide a fourth way of dealing with the frequency instability. However, we found that the magnitude of the probe tone required for the PID locking would drive the mechanics and alter the measurement results.

CHAPTER 6

Everyday Electromechanics at the fundamental mode

This chapter is based on the article Puglia et al. [76] and describes the room temperature measurements done in a 50 Ω environment. The article explores the applications of EEM, including low-loss inductor, parametric amplification, and remote cooling of mechanical motion. The extract follows bellow.

Light incident upon a massive body exerts a famously weak optomechanical force [52, 66, 28]. For the particular case of an oscillating mass with average speed v, Braginskiĭ and Manukin argued that the optomechanical coupling is suppressed by a factor of $(v/c)^2$, and is therefore a small quantity due to the enormity of the speed of light c [13]. Their realization that a cavity can resonantly enhance this coupling gave birth to the field of cavity optomechanics [13, 14, 7], in turn leading to experimental breakthroughs such as quantum ground-state cooling [79, 92, 16, 80, 56], quantum transduction [11, 3, 8, 98, 38, 61, 70, 25, 83], and detection of gravitational waves [2, 1]. Without the use of a cavity, substantial optomechanical coupling has nevertheless been achieved at optical frequencies [5, 6, 86, 51, 73, 91, 30]. However, at radio and microwave frequencies, cavity-free coupling has so far been impractically weak [87] unless piezoelectric materials [93, 64, 44, 69, 17, 18] or specialized experimental regimes involving high magnetic fields [21, 19, 20, 46] or Coulomb blockade [89, 50] are employed.

The weakness of cavity-free electromechanical coupling has been attributed to a mismatch, $Z_0/Z \ll 1$, between the small transmission-line impedance Z_0 and the large capacitive mechanical impedance Z [95]. This mismatch, in fact, re-expresses the suppression noted by Barginskiĭ and Manukin; for a linear geometry $Z_0/Z \sim v/c$. To see why, note that the gate impedance in a linear geometry is approximately $Z \sim 1/(\omega\epsilon\lambda)$, where λ is the mechanical wavelength. Using the relationship $\omega\lambda/(2\pi) = v_s$ leads to $Z_0/Z \sim v_s/c$, where we have approximated Z_0 by the impedance of free space, $Z_0 \sim \sqrt{\mu_0/\epsilon_0}$. In a two-dimensional parallel-plate geometry similar considerations yield $Z_0/Z \sim v_s\sqrt{A}/(cd)$, where A is the plate area and d is the plate separation. This is larger than the one dimensional case, but still small in practice. For instance, $v_s\sqrt{A}/(cd)$ would approach unity for macroscopic plates with $\sqrt{A} = 1$ m separated by 1 μm. Given both this fundamental mismatch and the absence of experimental evidence so far, it may be questioned whether cavity-free, capacitive electromechanical strong

coupling is possible at all. The purpose of this study is to affirmatively answer this question, and to explore physical and device implications.

Here we present a movable parallel-plate capacitor that reaches a strong-coupling regime where electromechanical coupling to a $50\ \Omega$ environment overwhelms internal mechanical dissipation. The experiment consists of two chips, a $\mathrm{Si_3N_4}$ membrane and a bottom electrode, flipped on top of each other. The membrane was produced from Si wafers covered with 1.1 GPa stoichiometric $\mathrm{Si_3N_4}$ on both sides. Using lithography, we define a window on the back of the wafer where $\mathrm{Si_3N_4}$ was removed through reactive ion etch. Most of the $\mathrm{Si_3N_4}$ on the front side of the wafer was also removed, leaving only a central square, which would become the 510-520 μm membrane, and smaller squares, which would become posts. The wafer was then dipped in KOH to etch the exposed silicon and release the membranes. We then evaporate 3 nm of Ti and 25 nm of Au on the released membranes. The electrode on the bottom chip was fabricated by evaporating 50 nm Pt on a high resistivity silicon wafer. We then evaporate 350 nm posts on the bottom chip, defining the separation distance between the bottom and top chip. The membrane chip was flipped on top of the electrode while carefully aligning the bottom and top posts. Finally, the two chips were glued with epoxy and bonded.

The samples were loaded into a vacuum chamber and kept at around 10^{-5} mbar and room temperature. Figure 6.2 uses data from Sample 1, Figs. 6.3 and 6.4 use data from Sample 2, and Fig. 6.5 uses data from Sample 3. This compact, room-temperature architecture achieves 30,000 times (45 dB) lower insertion loss and 10 times larger inductive bandwidth than a commercial piezoelectric device operating at similar frequencies. We use this platform to efficiently detect mechanical motion with an imprecision under $20\ \mathrm{fm}/\sqrt{\mathrm{Hz}}$, rivaling optical Michelson interferometers [73]. Implementing a back-action isolation scheme, we verify that mechanical motion thermalizes to the external environment, as expected for strong coupling, and observe radiative cooling of mechanical motion by a remote cryogenic load.

We identify two requirements for strong, cavity-free electromechanical coupling: *(1)* that, by definition, the total electromechanical coupling rate, $2g$ for a two-port device, exceed the internal dissipation rate κ_{in}, and *(2)* that, in practice, no antiresonance obscure useful circuit properties.

To achieve these requirements, we have devised a system consisting of a metallized $\mathrm{Si_3N_4}$ membrane chip flipped on top of an electrode chip, with each chip coupled to a $50\ \Omega$ transmission line (Fig. 6.1). The flipped pair of chips forms a movable capacitor $C(x)$ where x is a coordinate parameterizing the mechanical displacement (see Chapter 2). The electromechanical system is governed by the interaction Hamiltonian $H_{\mathrm{int}} = -\frac{1}{2}C(x)V^2$, where $V = V_{\mathrm{DC,S}} + V_{\mathrm{AC}}$ is the combination of a large static DC and small oscillating AC voltage. The AC voltage results in an oscillating electromechanical force $F_{\mathrm{em}} = C' V_{\mathrm{DC,S}} V_{\mathrm{AC}}$ which is parametrically enhanced by $V_{\mathrm{DC,S}}$ (here $C' = \partial C/\partial x$ evaluated at equilibrium). Decomposing the AC voltage into incoming and outgoing waves in the transmission line $V_{\mathrm{AC}} = V^+ + V^-$ reveals that there is a back-action contribution to F_{em} arising from the reflected wave. The constitutive capacitive relation $q = C(x)V$ can be differentiated to show that this back-action force is phase delayed, generating electromechanical damping at a rate

$$g = C'^2 V_{\mathrm{DC,S}}^2 Z_0/m, \tag{6.1}$$

where Z_0 is the transmission line impedance and m is the motional mass of the membrane. Although we find the distributed-element language convenient for describing our apparatus, we note that at our low radio frequencies accumulated phases in the transmission lines are

small, and the transmission line can be equivalently understood as a lumped-element resistor with resistance Z_0.

Requirement *(1)*, $2g/\kappa_{\mathrm{in}} > 1$, is analogous to reaching the high-cooperativity regime in cavity optomechanics and implies that dissipation is dominated by back-action damping from the environment. We therefore introduce an analogous "cooperativity" metric, $\mathscr{C} = 2g/\kappa_{\mathrm{in}}$. We achieve $\mathscr{C} > 1$ by maximizing C' with large typical membrane areas of $500 \times 500\ \mu\mathrm{m}^2$ and small typical membrane-electrode separations of $300\ \mathrm{nm}$. Note that for a given geometry, the maximum achievable V_{DC} is limited by instability (see Section 2.2).

Requirement *(2)* for preserving useful circuit properties is motivated by the unavoidable presence of an antiresonance due to the electrostatic gate. This is accomplished by detuning the mechanical resonant frequency Ω_m from the antiresonant frequency Ω_a. The mechanical resonance is shifted from its zero-voltage value Ω_0 according to

$$\Omega_m^2 = \Omega_0^2 - \Omega_e^2, \tag{6.2}$$

where $\Omega_e = \frac{C'' V_{\mathrm{DC,S}}^2}{2m}$ and $C'' = \partial^2 C/\partial x^2$. The antiresonance Ω_a^2 is voltage-tuned according to

$$\Omega_a^2 = \Omega_m^2 + \frac{g}{Z_0 C}. \tag{6.3}$$

Equation 6.3 indicates that, in our approach, strong antiresonance detuning is an automatic consequence of having large g. In fact, the antiresonance detuning $\Omega_a - \Omega_m \approx g(Z/Z_0)$ is controlled by Z/Z_0, which, as discussed above, is large in practice. Strongly detuning the antiresonance gives unobscured access to large effective mechanical inductance, a desirable feature for electrical circuits.

Such circuit can be measured using a lock-in amplifier for the probe tone and, when present, an arbitrary waveform generator was used for the pump tone. For the two-port measurement, the pump and probe tones were added to the coupled port of a directional coupler. The mainline

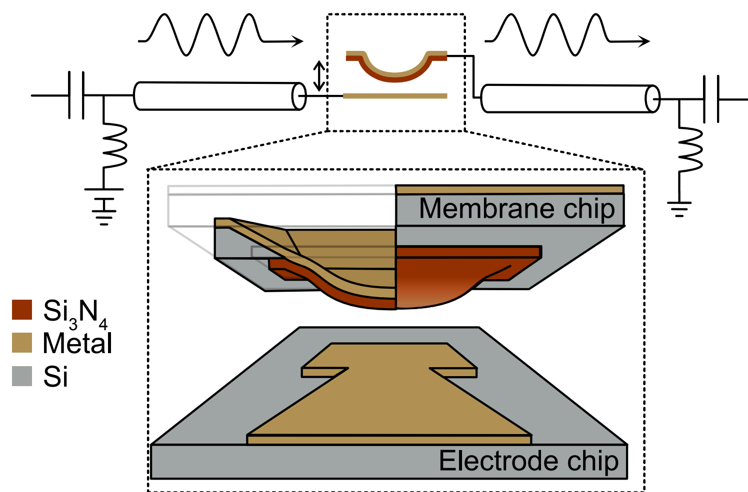

Figure 6.1: **Everyday electromechanics (EEM) setup.** A metallized Si_3N_4 membrane chip is flipped on an electrode chip and both are coupled to transmission lines, allowing the transmission S_{21} to be measured. The front left quadrant of the membrane chip is omitted from the schematics and only the contour lines are shown. A DC bias tunes the coupling between the transmission lines and the flipped chip.

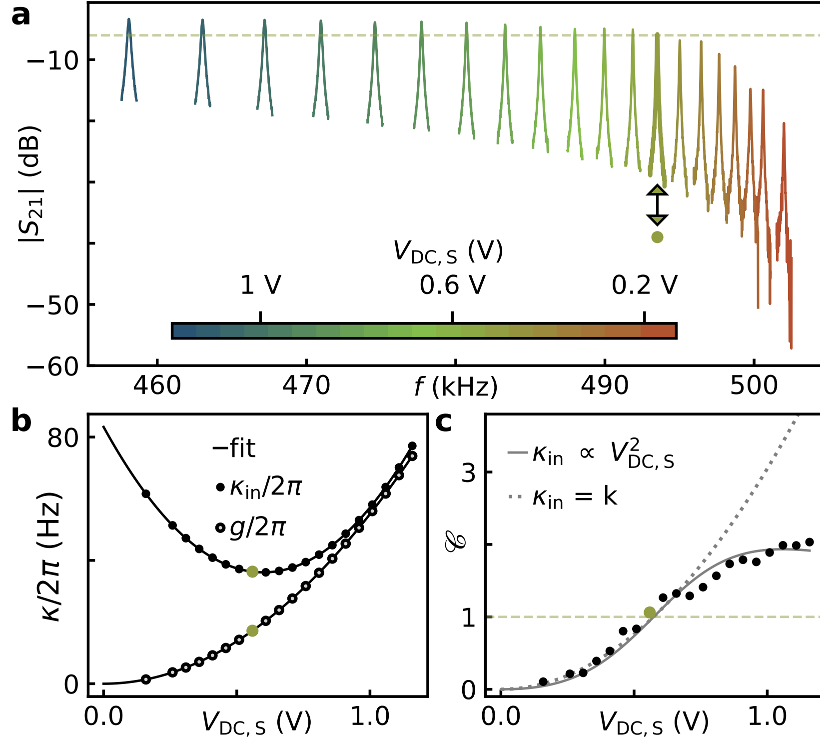

Figure 6.2: **Tuning from weak to strong electromechanical regime.** **a**, S_{21} transmission parameter around resonance for different voltages. The dashed green line indicates expected threshold transmission when the device is operated in the strong coupling regime $2g > \kappa_{\text{in}}$. **b**, External coupling g and internal coupling κ_{in} as a function of voltage. Green marker was calculated from the highlighted trace in **a**. The full lines represent the voltage dependence fits. **c**, Cooperativity $\mathscr{C}$ as a function of voltage, with the green marker calculated from the highlighted trace in **a**. The dashed green line shows $\mathscr{C} = 1$, above which the device is considered to operate in the strong coupling regime. The full line indicates the expected cooperativity based on the voltage dependence fit from **b**, while the dotted line indicates the expected cooperativity for a constant internal coupling.

was grounded by a 50 ohm resistor. This AC signal was added to a DC bias through a bias-tee and connected to the back of the membrane. The transmitted radio wave would travel from the electrode directly to the input of the lock-in amplifier. The two-port measurement was converted to one-port with a 180 degrees hybrid coupler. The hybrid coupler recombines the scattering matrix elements with a phase, canceling the transmitted contributions and returning the reflection parameter S_{11} at the output port. The incoming signal follows a similar path as for the two-port measurement, passing through the mainline of an extra directional coupler. Through the coupled port of this directional coupler, we can read out the reflected wave from the sample. It is also worth to mention that the data presented in this paper was acquired with a table-top setup occupying about 1 m^2. However, this space can be greatly reduced.A dedicated low loss inductor would require about 15x10x5 mm^3 of volume for a vacuum-sealed enclosure with an SMT connection for V. A rough estimate suggests that the parametric amplification with (or without) back-action isolation can be carried out in a 40x40x20 mm^3 enclosure with SMA connectors for V.

Using this setup, the strength of electromechanical coupling is experimentally assessed by measuring the transmission coefficient S_{21} for different DC bias voltages. For $V_{\text{DC}} = 0$ V, a narrow, resonant peak in transmission is observed, suggesting weak but nonzero electrome-

chanical coupling at low bias (Fig. 6.2a). Increasing $V_{\rm DC}$ causes the resonance to increase and widen, indicating a growth in electromechanical coupling. For large voltage ($\gtrsim$ 0.4 V), the resonant transmission becomes voltage independent, saturating at a value slightly below unity.

Fitting S_{21} to Lorentzian lineshapes, we extract g and $\kappa_{\rm in}$, with $\kappa_{\rm in}$ including both intrinsic mechanical loss and any parasitic resistive losses [19]. Figure 6.2b shows that g depends quadratically on applied voltage over the entire measurement range, as qualitatively expected from Eq. 6.1. However, we consistently find that external coupling is minimized at non-zero DC voltage, presumably due to interfacial charges, motivating the use of a shifted bias $V_{\rm DC,S} = V_{\rm DC} - V_0$, where V_0 is sample dependent. The voltage offset is determined by fitting $g(V_{\rm DC,S})$ to Eq. 6.1 with $V_{\rm DC,S} = V_{\rm DC} - V_0$. Internal dissipation is non-monotonic in $V_{\rm DC,S}$, reaching a minimum near 0.4 V and growing for large voltage, eventually matching the growth in g, which is the origin of the saturation in resonant transmission at large voltages. We speculate that the quadratic voltage-dependence of $\kappa_{\rm in}$ is due to parasitic inline resistance from the electrodes [19]. The relative voltage shift between $\kappa_{\rm in}$ and g is not understood. The minimum internal dissipation is limited to around 36±8 Hz for this sample, but reaches values down to 5±2 Hz for other samples (see Appendix B).

The competition between coupling and dissipation is summarized with the "cooperativity" metric $\mathscr{C} = 2g/\kappa_{\rm in}$ (Fig. 6.2c). As voltage is increased $\mathscr{C}$ increases from a small value eventually crossing the $\mathscr{C} > 1$ threshold for strong coupling. This signals that the light-matter interaction has entered into a regime where mechanical motion is damped primarily by radiation in the leads. To the best of our knowledge, this is the first reported device to reach cavity-free capacitive strong coupling between electromagnetic radiation and mechanical motion.

Strong-coupling everyday electromechanics opens up new avenues for electromechanical devices in regimes that are challenging for existing technology. To explore this, Fig. 6.3a shows a comparison between the everyday electromechanics (EEM) device and the commercial quartz crystal oscillator CC1V-T1A operating at a similar frequency. EEM shows an insertion loss 30,000x (45 dB) lower than the crystal. Both systems present an antiresonance as qualitatively expected from a Butterworth-van Dyke model [41, 95]; which includes a series RLC circuit ($R_{\rm eff}$, $L_{\rm eff}$, $C_{\rm eff}$) in parallel with a gate capacitor (C). The gate capacitance is defined by the geometry of the metallized membrane at an equilibrium distance from the electrode. In terms of measurable and fitted variables it is determined by:

$$C = \frac{g}{Z_0(\Omega_a^2 - \Omega_m^2)}. \tag{6.4}$$

Similarly, the series RLC circuit can be defined as:

$$C_{\rm eff} = \frac{C^2 V_{\rm DC,S}^2}{d^2} \frac{1}{m\Omega_m^2} \tag{6.5}$$

$$L_{\rm eff} = \frac{1}{\Omega_m^2 C_{\rm eff}} \tag{6.6}$$

$$R_{\rm eff} = \kappa_{\rm in} L_{\rm eff}. \tag{6.7}$$

To explain the shape of the EEM antiresonance, an extra shunt resistor (R_s) is added in parallel to the Butterworth-van Dyke model. In Fig. 6.3a, we fit the transmission coefficient for the phase of the transmission coefficient as well as C, $\kappa_{\rm in}$, g, Ω_m, and R_s (for EEM). The effective circuit parameters are then calculated as defined above.

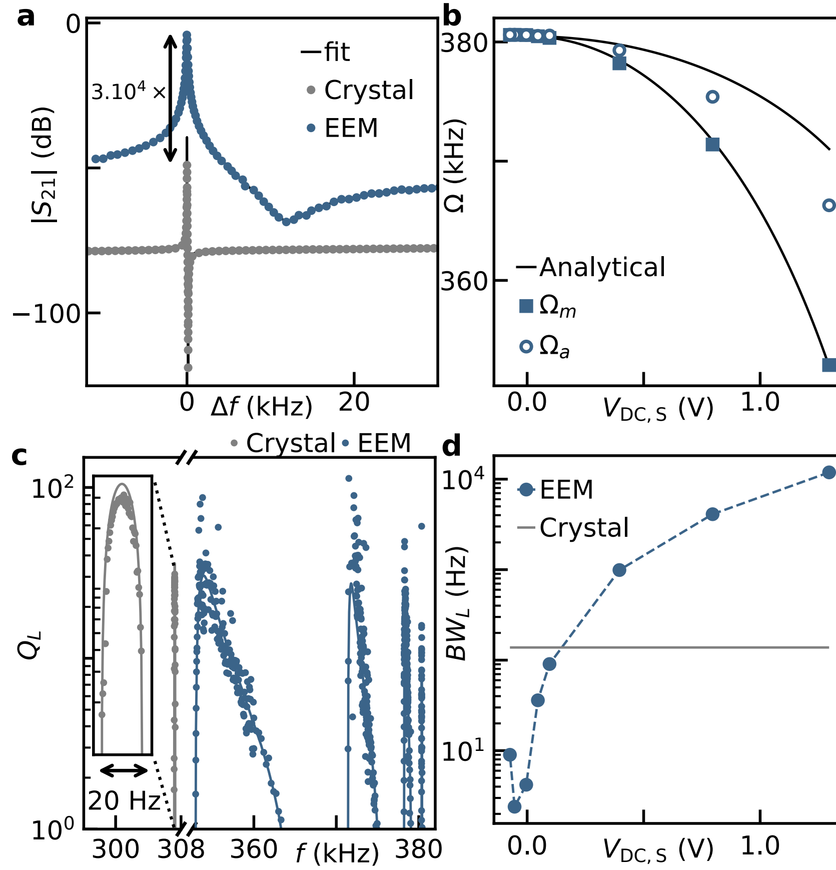

Figure 6.3: **Comparison with a commercial device.** **a**, S_{21} around the resonance and antiresonance for the crystal and the EEM at $\mathrm{V_{DC}} = 1$ V. Full line represents a fit. **b**, Antiresonance Ω_a and resonance Ω_m voltage dependence. The full line represents a fit of the voltage dependence from the mechanical resonance and expected antiresonance dependence based on this fit. **c**, Inductor quality factor Q_L data (marker) and fit (full line). The inset shows the commercial quartz crystal (CC1V-T1A) resonance. **d**, Inductive bandwidth BW_L, defined by the frequency range over which $\mathrm{Im}(Z) > 0$ for a fixed $V_{\mathrm{DC,S}}$. Points are calculated from the data in **c**, and the line is a guide to the eye. Horizontal line indicates inductive bandwidth of the crystal.

In Fig. 6.3b, we fit the squared resonance frequencies Ω_m^2 to Eq. 6.2 with d and Ω_0 as fit parameters. The voltage shift is a fit of Eq. 6.1 to the voltage dependence of g. The membrane mass m is calculated from the sample's design and optically-measured geometry. $C''(d, V_{\mathrm{DC,S}})$ is calculated numerically accounting for the equilibrium deflection of the membrane due to $V_{\mathrm{DC,S}}$ (see Chapter 2 Eq. 2.12).

Both the resonant and antiresonant frequencies are voltage tunable. At low voltages, there is very little detuning of the antiresonance from the resonance. As voltage increases, the frequency of the resonance decreases faster than that of the antiresonance, increasing the detuning between the two (Fig. 6.3b). We fit the squared resonance frequencies Ω_m^2 to Eq. 6.2 with d and Ω_0 as fit parameters. The voltage shift is a fit of Eq. 6.1 to the voltage dependence of g. The membrane mass m is calculated from the sample's design and optically-measured geometry. $C''(d, V_{\mathrm{DC,S}})$ is calculated numerically accounting for the equilibrium deflection of the membrane due to $V_{\mathrm{DC,S}}$ (see Chapter 2 Eq. 2.12). The fit yields a zero-voltage frequency Ω_0 is within 0.07% of expectations based on fabrication parameters, and a zero-voltage separation distance $d = 320$ nm, within 20 nm of the design value. The similarity between

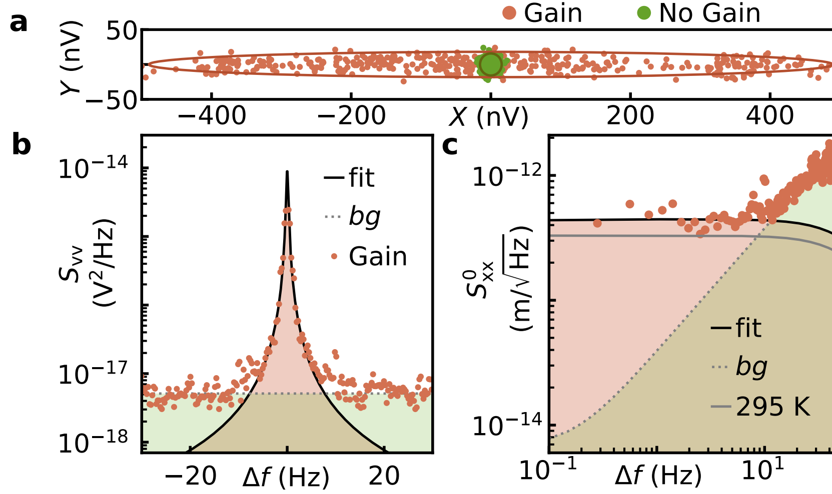

Figure 6.4: **High-precision position measurements.** **a**, demodulated X and Y quadratures for EEM with (orange) and without (green) parametric gain. The full line represents 4x the standard deviation of the data. **b**, the voltage spectral density S_{VV} for the parametrically amplified trace shown in **a**. The solid line is a fit to a Lorentzian with an offset bg (dotted line). The green shading indicates the voltage noise of the measurement amplifier and the orange shading indicates the excess noise due to thermomechanical fluctuations. **c**, Position imprecision inferred from **b** using Eq. 6.8. The full gray line represents the expected contribution of thermomechanical fluctuations at 295 K.

target parameters and fitted values demonstrates good fabrication control. Equation 6.3 predicts the voltage dependence of the antiresonant frequency to within 1.2% with no free parameters, although the experimental antiresonance systematically depends more strongly on voltage than expected.

Given the prevalence of quartz crystal oscillators in electrical engineering, it is natural to view EEM as a circuit element characterized by a lumped-element impedance Z. Transforming the measured scattering parameters into an impedance reveals an inductive region ($Z \approx \mathrm{Im}(Z) > 0$) at frequencies between the resonance and antiresonance (Fig. 6.3a). We quantify the quality of this effective inductance with the metric $Q_L = \frac{\mathrm{Im}(Z)}{\mathrm{Re}(Z)}$ calculated for the inductor region ($Im(Z) > 0$). The imaginary and real projections require a fit for the phase of the transmission coefficient. At the beginning of the inductive region, $Re(Z)$ and $Im(Z)$ are very small and the error of the phase fit can make Q_L diverge. This can be observed in Fig. 6.3c in which a few data points present much larger Q_L than the fit. The inductor loss metrics reveals $Q_L \approx 30$, which is comparable to that of the commercial quartz crystal.

EEM maintains this Q_L over more than 25 kHz of tunable bandwidth by adjusting the DC voltage. At fixed DC voltage EEM has an instantaneous inductive bandwidth BW_L surpassing $10\ \mathrm{kHz}$, which is two orders of magnitude larger than the commercial crystal (Fig. 6.3d). Thus, EEM shows promise as a compact, low insertion loss, high Q_L, and wide band inductor for electrical engineering.

A fundamental consequence of reaching strong electromechanical coupling ($\mathscr{C} > 1$) is that mechanical motion thermalizes to radiation in the environment. However, at our low operating frequencies, thermomechanical fluctuations are obscured by technical noise associated with the measurement chain. To overwhelm this technical noise, we introduce a parametric drive at twice the mechanical resonant frequency while measuring demodulated ($X(t)$, $Y(t)$)

quadratures at the mechanical resonant frequency. As shown in Fig. 6.4a, the introduction of a parametric drive causes a substantial gain in the X-quadrature noise, vastly exceeding the technical noise of the measurement, and no significant change in the Y quadrature, as expected for this pumping configuration. The amplified X-quadrature is strongly peaked at mechanical resonance, consistent with the expected Lorentzian profile of amplified mechanical noise (Fig. 6.4b).

In the high-gain limit, the voltage fluctuation can be directly converted into equivalent undriven position imprecision S^0_{xx} using the relation

$$S_{\mathrm{VV}} = gm\Omega_m^2|G(f)|^2 S^0_{\mathrm{xx}}, \tag{6.8}$$

where $G(f)$ is the frequency-dependent gain of the quadrature being measured

$$G(f) = \frac{2\pi f - \frac{i\kappa}{2}}{2\pi f - i\kappa/(2G_A)} \tag{6.9}$$

where G_A is the gain of the amplified quadrature, as discussed in the Section 2.5.

Near mechanical resonance, S^0_{xx} is dominated by mechanical fluctuations, and we find that technical noise contributes with less than $20\ \mathrm{fm}/\sqrt{\mathrm{Hz}}$ of position imprecision, which is comparable to state-of-the-art cavity-free optical interferometers working towards ground state cooling [73]. However, the thermomechanical fluctuations associated with the Lorentzian fit are equivalent to a temperature of $568 \pm 15\ \mathrm{K}$, far exceeding room temperature. This value is compatible with independent measurements of the electrical back-action noise of the electronics in our measurement setup, determined by attaching several different external resistors to the apparatus input while measuring voltage noise at the output. We found an input voltage noise of $4\ \mathrm{nV}/\sqrt{\mathrm{Hz}}$, matching the manufacturer's specification for our instrument, and an input current noise of $25\ \mathrm{pA}/\sqrt{\mathrm{Hz}}$. In the un-isolated setup, we estimate that this current noise will heat mechanical motion to a temperature of approximately $484\ \mathrm{K}$, close to the excess thermomechanical noise measured in Fig. 6.4. Thus, unlike optical interferometers, our measurement apparatus gives substantial back-action noise.

To address this problem, we have devised a simple back-action isolation scheme to protect the mechanical oscillator from measurement noise. The input signal is added through the main line of a directional coupler and reflection is measured through the coupled port (Fig. 6.5a). Attenuation from the coupled port reduces measurement back-action at the expense of increasing imprecision. The main line carries predominantly the voltage fluctuations from a reference $50\ \Omega$ resistor which, in the limit of strong electromechanical coupling, controls the equilibrium temperature of the mechanical resonator. As a consequence, cooling the reference resistor is expected to radiatively cool mechanical motion. Voltage spectral densities measured in the back-action isolation configuration exhibit a Lorentzian thermomechanical fluctuation peak which is reduced compared to the un-isolated setup (*cf.* Fig. 6.5b and Fig. 6.4a), as expected since now the gain is attenuated by the coupled port. Cryogenically cooling the remote, $50\ \Omega$ load noticeably decreases the peak voltage spectral density, giving an initial indication that the mechanical temperature is lowered. This observation can be quantified by calculating a temperature-equivalent area A_{eq} under the thermomechanical Lorentzian which measures the mechanical temperature T_m,

$$A_{\mathrm{eq}} = G_{\mathrm{eq}} T_m - \eta T, \tag{6.10}$$

where η is the insertion loss from the membrane to the voltage measurement and $G_{\mathrm{eq}} = \eta G_A$ is the net mechanical gain. Fig. 6.5c shows the numerically-integrated area as a function of

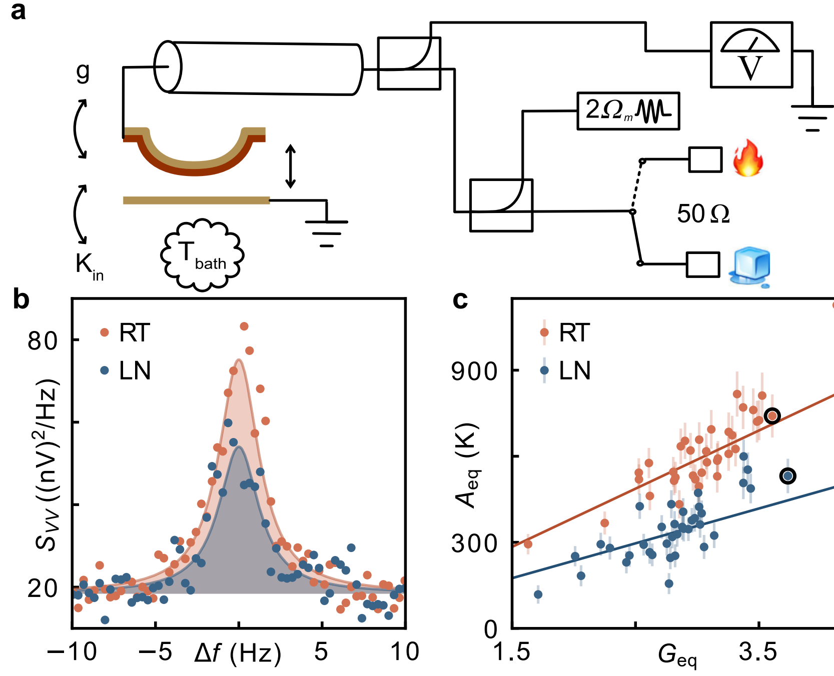

Figure 6.5: **Back-action isolation.** **a**, EEM circuit in reflection and back-action isolation mode. The temperature of the external port is determined by a 50 Ω resistor at LN (ice cube) or room (fire) temperature. **b**, Voltage spectral density for an EEM device thermalized to RT and LN. The full line represents a Lorentzian curve as a guide to the eye. The thermomechanical fluctuations are proportional to the area between the trace and the background, as indicated by the shading. **c**, Area under the curve of the thermomechanical fluctuations for different apparent gains. The circle markers correspond to traces shown in **b**. The full line represents a fit of the gain dependence.

$G_{\rm eq}$, where the gain is independently measured with a pilot tone for each experimental run. Fitting to Eq. 6.10 gives $T_m = 281 \pm 7$ K for the room temperature load, a reasonable value as all system components are in thermal equilibrium and the expected mechanical temperature T_m is 295 K. The same fitting procedure for the cold load yields $T_m = 171 \pm 7$ K. For the cold load, the expected mechanical temperature is given by $T_m = (2g/\kappa)T_{\rm in} + (\kappa_{\rm in}/\kappa)T_{\rm RT}$ where $T_{\rm RT} = 295$ K and $T_{\rm in}$ is the input radiation temperature. The parameters g, $\kappa_{\rm in}$, and κ are fixed from measured scattering parameters and $T_{\rm in} = 105$ K from the temperature of liquid nitrogen and the measured insertion loss from the cold load to the sample. The expected value of 177 K, which is within the error for the measured value. This demonstrates the radiative cooling of a room-temperature mechanical resonator by a remote cryogenic load.

The error bars presented in Fig. 6.5c are given by the sensitivity of the Dicke radiometer, a common metric for thermally-emitted electromagnetic radiation. For an ideal Dicke radiometer, the standard deviation of the area (σ_A) is:

$$\sigma_A = \sqrt{\frac{A_a}{N_a/2} + \frac{A_w}{N_w/2}}, \tag{6.11}$$

where $A_{a/w}$ is the area contribution from the amplified thermomechanical fluctuations/white noise, and $N_{a/w}$ is the number of independent samples contributed by the same sources. The white noise is uncorrelated, so N_w is simply the length of the trace divided by the sampling time (t_s). However, the amplified thermomechanical fluctuations are correlated and N_a must

correct the independent number of points, dividing it by N_{corr}:

$$N_{\mathrm{corr}} = \frac{2}{\kappa/G_A t_s}, \tag{6.12}$$

where κ/G_A is the bandwidth. It is interesting to note that the spread of the points in Fig. 6.5c is not compatible with statistical errors. Rather, we believe it originates from gain instabilities during individual measurements. Provided that these gain instabilities are cured, EEM could be a competitive 50 Ω matched amplifier and would achieve noise performance comparable to radio-to-optical receivers [8]. Alternatively the EEM amplifier can be operated in high impedance environment, in which gain instabilities are not observed (see Supplement).

Summarizing, we have reported a platform to achieve cavity-free capacitive strong electromechanical coupling in an all-electric device. This voltage-tunable coupling reaches cooperativity $\mathscr{C} > 1$ for V_{DC} as low as 0.5 V. From a circuit element perspective, EEM presents a region of inductive behavior that is wider and less lossy than in commercial quartz crystals. These features could be useful in applications that require large, low-loss inductance, such as a compact step-up transformer for noise matching to transistor amplifiers. We further demonstrate parametric amplification of the EEM, and resolve thermomechanical fluctuations. Amplifications results in a low equivalent position imprecision $S_{\mathrm{xx}}^{0} < 20\ \mathrm{fm}/\sqrt{\mathrm{Hz}}$, suggesting future applications in sensing. In this configuration, mechanical motion was heated by electrical back-action by more than 300 K. A back-action isolation scheme removed the excess heating, enabling the cooling of mechanical motion to 171 K with a remote cryogenic resistor. In addition to the possible applications mentioned above, we expect our approach to be generally useful in environments that are challenging for optical cavities or superconducting resonators.

CHAPTER 7

Everyday Electromechanics at the high order modes

High order resonant modes can offer inumerous advantages compared to the so far studied fundamental mode, as for example, higher sensitivity, faster measurements, and better noise performance [34, 105, 24]. Besides, these mechanical modes can couple to a device under test or another resonator, a common design applied in MEMS filters and inertial sensors [55, 100, 102, 40, 77, 88, 68, 67, 72]. In cavity optomechanics, higher order modes are mainly used to transduce mechanical motion into light and vice-versa [10, 39, 31, 101]. A classical example is the usage of the mode (1,2). While one lobe is illuminated by light, the other is free to probe the environment. The symmetry of the mode ensures that the interactions on one lobe are mirrored onto the other, providing an indirect, non-perturbative measurement of the environment. Mechanical modes can also couple to other mechanical modes in the same resonator due to the presence of nonlinearities. This topic has drawn special attention after the characterization of nonlinear dynamics in an electrostatically coupled microbeam array, the observation of mode localization in an array of cantilevers, and the observation of strong coupling in CNTs [15, 85, 95, 54, 27, 33].

Regardless if measured independently, coupled to a resonator or another mechanical mode, mechanical out-of-plane vibrational modes of 1- and 2-dimensional structures carry an intrinsic fourier-like spatial information. This advantage has already being exploited to perform mass spectrometry on single proteins by monitoring vibrational modes of a cantilever [29, 104, 63, 26, 36, 37]. By measuring the shift in frequency of several modes in these systems, it is possible to determine the added mass with atomic resolution and its spatial distribution. We will now like to expand this idea from a 1-dimensional cantilever to a 2-dimensional membrane and move from mass to electrical charge analysis.

7.1 Charge Distributions

Consider we have a single charge q in a flip-chip at position y_q, z_q. We can determine its location by measuring the resonance frequency shift of modes (1,1) and (2,1):

$$\frac{\Delta\omega_{11}}{\Delta\omega_{21}} = \frac{2\phi_{11}^2(y_q, z_q)}{\phi_{21}^2(y_q, z_q)} \tag{7.1}$$

where ϕ_{ab} is the mode shape for mode (a, b). Using Eq.2.9, we can determine the position of the charge as

$$y_q = sin^{-1}\Big(\sqrt{\frac{\Delta\omega_{11}}{2\Delta\omega_{21}}}\Big)\frac{L_y}{\pi}, z_q = sin^{-1}\Big(\sqrt{\frac{\Delta\omega_{11}}{2\Delta\omega_{21}}}\Big)\frac{L_z}{\pi}. \tag{7.2}$$

However, the location of multiple charges cannot be solved analytically as the system of equations becomes underdetermined. In this case, the charge distribution can be estimated by using machine learning algorithms.

A cost function describes how well the charge distribution model $V_{\mathrm{DC}}(y, z)$ matches the measured frequency shifts based on Eq 2.11

$$C = \left(\sum_{ab}\int\frac{V_{\mathrm{DC}}(y,z)\phi_{ab}^2(y,z)}{2\rho h\epsilon_0\Omega_0^2 ab\pi^2}dydz - \frac{\Delta\omega_{ab}}{\Omega_0}\right)^2. \tag{7.3}$$

By minimizing the cost function, it is possible to estimate the charge distribution.

7.1.1 Adaptive Learning

Machine learning provides us with several algorithms to minimize the cost function. The performance of the algorithms is case-dependent, therefore it is necessary to verify which algorithm performs better for the given problem [81, 74, 59]. In this thesis, we will focus on the algorithm called adaptive learning. The algorithm is as follow

$$V_{\mathrm{t+1}} = V_{\mathrm{t}} + \mu(V_{\mathrm{t}} - V_{\mathrm{t-1}}) - l\nabla C(V_{\mathrm{t}} + \mu(V_{\mathrm{t}} - V_{\mathrm{t-1}})) \tag{7.4}$$

where V_{t} is the charge distribution $V_{\mathrm{DC}}(y, z)$ at computational time t, μ is the learning momentum, and l is the learning step. Since the step is proportional to the gradient of the cost function (∇C), this class of algorithm is called gradient descent. Contrary to Nesterov, the learning step l in adaptive learning decreases as t increases. This way, it is possible to make finer changes to the final charge distribution.

We input a random charge distribution ($V_{\mathrm{t=0}}$) and empirically determine the parameters μ and l by analyzing the change in the cost function [90, 47]. A too small learning step l or momentum μ takes too long to converge, however, if these parameters are too big, the algorithm does not converge. Once the parameters are determined, the reconstruction algorithm returns the distribution $V_{\mathrm{DC}}(y, z)$ that minimizes the cost function.

7.1.2 Simulation

The feasability of the method was verified by simulating the charge distribution $V_{\mathrm{DC}}(y, z)$, calculating the respective $\Delta\Omega_{ab}$, and feeding them to the reconstruction algorithm. Figure 7.1(a) and (b) show simulated charge distributions in a Hall bar under the bottom left quadrant of a 52x55 μm membrane. In gray we see the simulated substrate (no charge) and in yellow the electrodes and charge puddles. The resolution is defined by the size of the membrane and the number of modes use for the reconstruction. To better estimate the resolution, let us take the first mode of a string with length L as an example ($\phi_1 = sin(\frac{\pi y}{L})$). The frequency shift is proportional to $sin^2(\frac{\pi y}{L})$ and is thus zero at the edges and nodal points. The maximum change in amplitude occurs at the inflection point, however, the algorithm can easily distinguish smaller changes in amplitude, resulting in a sampling frequency of approximately 6× the mode

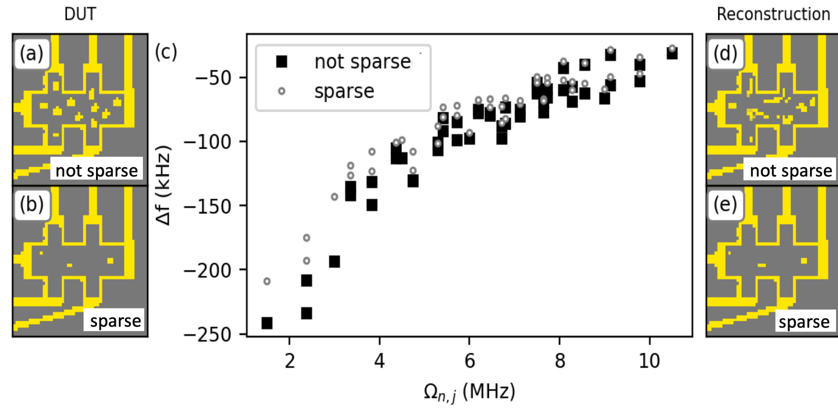

Figure 7.1: (a) and (b) Simulated charge distributions in a Hall bar. A pixel represents 0.5 μm. (c) Frequency shifts of the mechanical resonance for the two distributions shown in (a) and (b) for the first 7×7 resonant modes. (d) and (e) Reconstructed charge distribution based on the frequency shifts in (c).

shape frequency. For the first mode, this criterium implies reliable detection of changes in amplitude at 5 points. Repeating this procedure for the first 7 resonant modes and excluding duplicated measurement points, we obtain a list of unique points that produce measurable shifts in the frequency. This criterium gives us a resolution of around 0.47 μm/pixel for a 52x55 μm membrane. Therefore, the bottom electrode was pixelated for the simulation with a 0.5 μm pixel size. It is important to point out that, very high order modes might not produce measurable changes in amplitude at all unique points, so the resolution would have to be experimentally verified.

The frequency shift Δf of two charge distributions up to mode number 7 in each direction is shown in Fig. 7.1(c). As the mode number increases, the frequency shift Δf decreases and both even- and odd-index modes show non zero Δf, as the flip-chip configuration is not 90° symmetric. A clear difference between the "sparse" and "not sparse" distributions can be observed up to the highest order modes, indicating a good sensitivity up to mode number 7.

Figure 7.1(d) and (e) show the reconstruction charge distribution based on the frequency shift Δf shown in Fig. 7.1(c). The charge of the electrodes (1 V) and substrate (0 V) was fixed and the charge was reconstructed only inside the region of interest: the hall bar area delimited by the electrodes. This is reasonable limitation as it is very easy to optically measure roughly where the electrodes and substrate are, allowing a delimitation of a region of interest. The analysis takes around 2 minutes to run in a Mac Book Pro laptop with 16 GB of memory and a 2 GHz Quad-Core Intel Core i5 processor. The reconstructed sparse distribution is in very good agreement with the input charge distribution showing an average accuracy/pixel of 99.1 %, while the "non sparse" distribution shows an accuracy/pixel of 73.6 %.

7.2 Multimode Measurements

This section aims to introduce the preliminary results of the multimode analysis. We focused on measuring the frequency of high order modes based on two techniques: scattering parameters, in which modes are independently measured, and two-tone experiment, in which nonlinearities couple higher order modes to the fundamental mode.

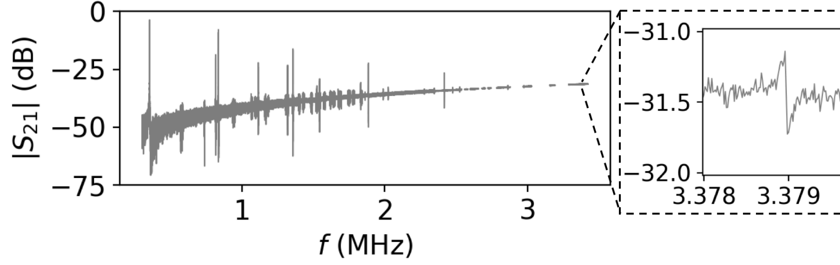

Figure 7.2: Scattering parameter of the probe tone as a function of pump frequency. Inset shows last measured mode.

7.2.1 Scattering Parameters

The technique presented in section 5.1.1 can be extended for measuring scattering parameters S_{11} or S_{21} at higher frequencies. The measurement of the S_{21} coefficient is preferred, as it presented better signal to noise ratio (see Fig.5.1). Figure 7.2(a) presents the S_{21} coefficient for a 520 μm square membrane flipped on a square electrode and measured at different frequencies. Given the symmetry of the flipped-chip, the C' integral in Eq.6.1 cancels out which makes the external coupling g to even modes very weak, rendering these modes indectable. Odd-index modes present an excellent coupling g and can be detected up to the order of (15,1). The inset zooms in around the last measured peak at 3.38 MHz and an amplitude of 0.23 dB. No higher order modes were detected, suggesting that the transmission of higher order peaks is bellow background. To the best of our knowledge, this is the highest reported all-electrical measurement of a resonant mode in a membrane. We would to further extend this achievement by using two-tone spectroscopy.

7.2.2 Two-Tone Spectroscopy

Two-tone spectroscopy is a technique based on the non-linear response largely exploited in fields from material science to quantum computing. However, this technique remains still relatively unexplored in the field of MEMS. There are two important types of nonlinearities in a flip-chip: actuation nonlinearity and geometric nonlinearity. The first emerges directly from the third order term in the Taylor expansion of the electric potential (Eq.2.2). The latter comes from the longitudinal stress generated by the elongation of the membrane under V_{AC}, which causes an increase in the tensile force. The time-averaged tension on the membrane is proportional to u_1^2, which becomes a significant term for large V_{AC} [103]. These nonlinearities create an intermodal coupling when two mechanical modes are simultaneously excited, changing the damping and adding a nonlinear stiffness α to the equation of motion Eq.2.17:

$$m_1\ddot{x}_1 = -m_1\Omega_{m1}^2 x_1 - m_2\kappa_{\mathrm{in},1}\dot{x}_1 - \alpha_1(x_1,\dot{x}_1,\ddot{x}_1,x_2,\dot{x}_2,\ddot{x}_2)m_1x_1 + F_{\mathrm{em}}, \tag{7.5}$$

$$m_2\ddot{x}_2 = -m_2\Omega_{m2}^2 x_2 - m_2\kappa_{\mathrm{in},2}\dot{x}_2 - \alpha_2(x_1,\dot{x}_1,\ddot{x}_1,x_2,\dot{x}_2,\ddot{x}_2)m_2x_2 + F_{\mathrm{em}}. \tag{7.6}$$

The lowest order correction to the stiffness reported to be significant in clamped structures has the form $\alpha_1 = ax_1^2 + bx_2^2$ [57, 58, 103], introducing the coupling term $(x_2^2x_1)$ and a cubic nonlinear stiffness (x_1^3), which originates the Duffing nonlinearity. The first term, adjusts the spring constant, while the second forces the flip-chip to find a new equilibrium position, similar to the electrostatic spring constant effect. Therefore, driving a higher order mode (x_2) alters the fundamental mode (x_1).

The change in the fundamental mode was observed by tracking the amplitude of a probe tone 5 Hz redshifted from the fundamental resonant frequency. A pump tone scans the frequency

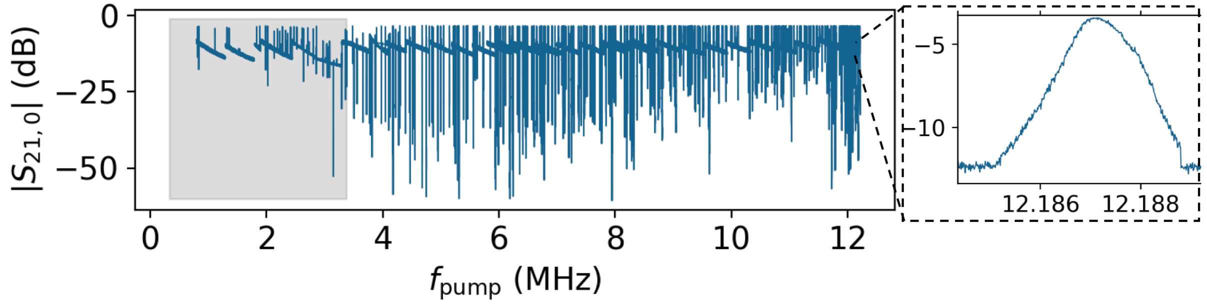

Figure 7.3: Scattering parameter with probe tone at the fundamental mode $S_{21,0}$ as a function of pump tone frequency. The gray shaded area indicates the measurement range in Fig.7.2. Inset shows last measured mode.

space $(f > \Omega_m)$. When the pump tone hits the frequency of the higher order mode x_2, it drives the mode incresing the coupling term. The fundamental mode lowers its frequency, which is detected by the change in the amplitude of the probe tone. The measurement setup is similar to the one introduced in Sec.5.1.1, with the pump tone added through the coupled port of a directional coupler instead of the parametric amplification tone.

Figure 7.3(a) shows the transmission coefficient of the probe tone $(S_{21,0})$ as a function of frequency of the pump tone. The scan starts close to the second odd mode and has, in principle, no limitation on the number of higher order modes. Here we show evidence of detecting a mechanical mode of the order (49,1) (see inset). This is a much higher order mode as detected in the scattering parameter measurement and, to the best of our knowledge, 5$\times$ higher than the highest previously reported mechanical mode on a membrane. The change in amplitude due to the detected mode is far above the background, presenting an astonishing signal to noise ratio and indicating that even higher order modes should be detectable. Unfortunately, the membrane collapsed shortly after this mode was measured, as the applied voltage was too high. Therefore, it was not possible to repeat the measurement at low voltage, which would provide the necessary data for reconstructing the charge distribution.

CHAPTER 8

Conclusion

EEM is a very sensitive and versatile platform that requires only AC and DC voltages applied to a flip-chip. A strong, tunable electromechanical coupling g is achieved and characterized by measuring the scattering parameters S_{11} and S_{12}. At the mechanical resonant frequency, a change in the scattering parameter is observed and indicated a weak electromechanical coupling g at low DC voltage and a large g at 1 V DC voltage. With the help of a cooperativity metric $\mathscr{C}$, we identify the transition to strong coupling regime in which the coupling to the itinerant radiation in the leads dominates over the internal dissipation. This regime opens new avenues for the development and application of MEMS without requiring cavities, high magnetic fields, or special materials.

The performance of the EEM was benchmarked against a commercial quartz crystal oscillator, demonstrating significantly lower insertion loss, better inductor quality factor, and higher inductor bandwidth. Hence the device proves to be a valuable candidate for low-loss wide-band inductors for electrical engineering applications. Furthermore, EEM was parametrically driven, enabling the electromechanical fluctuations to overcome the technical noise in the setup. From the driven voltage spectral density, a position imprecision was calculated revealing a sensitivity that rivals modern interferometry. In this transmission setup, the flip-chip was warmed up beyond room temperature due to back-action. A simple back-action isolation scheme based on a reflection setup thermalized the device to the temperature of the reference resistor, enabling remote cooling of mechanical motion.

EEM was also operated at high impedance environments revealing lossless transmission, but higher damping effects. The parametrically amplified quadrature is stable over extended periods, demonstrating the potential usage of EEM as an amplifier. Cooling the flip-chip to LN temperatures reduces the internal dissipation, thereby increasing the coupling ratio and pushing the device deeper into the strong coupling regime. However, it also increases the frequency shift of the mechanical resonance due to higher molecular adsorption rate to the membrane. To mitigate this, three strategies were successfully implemented: a high input impedance environment to leverage resonance stability, active cooling to counterbalance the adsorption frequency shifts, and short acquisition times with low-pass filtering. The subsequent voltage spectral density measurements revealed that the mechanical resonator thermalized to the theoretical expectations.

The last applications investigated in this thesis refer to higher order modes. A method for charge distribution reconstruction was proposed and its feasibility was validated through

simulations. The required frequency shifts were found through scattering parameters and two-tone spectroscopy measurements. Two-tone spectroscopy revealed astonishing sensitivity and significantly enhanced the detection range, enabling the characterization of modes of the order (49,1) and opening the doors to so far unexplored high order regimes. Further measurements need to be conducted to set a bound to the highest measurable mode with this technique and to have a complete dataset necessary for charge reconstruction.

The experimental results and methods presented here lay a strong foundation for future exploration of EEM. With the technique established, it would be interesting to investigate the electromechanical coupling to samples with challenging charge configurations. Reasonable candidates would be a chain of superconducting interference devices (SQUID) or Josephson junction arrays (JJA). Characterizing an array with two SQUIDs would calibrate the performance of EEM under charge tunnelings, while characterizing JJAs would give insight into not yet understood charge rearrangement in insulating systems. The dynamics in such systems are remarkably complex: instead of having a fixed location, electrons move around the lattice and eventually localize due to interactions with other electrons or due to the interference of paths in the lattice. A recent theoretical study calculated the response of a disordered system to a time-dependent perturbation and found that perturbations over a time scale τ rearrange the charges over a length scale $ln(\tau)$ [43]. This discovery contradicts our current understanding of Anderson, weak, and many-body localization and sets a time limit to the control of localized phases. However, the finding has not been confirmed due to experimental challenges, making it a perfect testbed for an EEM study.

Bibliography

[1] Benjamin P Abbott, Richard Abbott, TDe Abbott, MR Abernathy, Fausto Acernese, Kendall Ackley, Carl Adams, Thomas Adams, Paolo Addesso, Rana X Adhikari, et al. Observation of gravitational waves from a binary black hole merger. *Physical review letters*, 116(6):061102, 2016.

[2] Alex Abramovici, William E Althouse, Ronald WP Drever, Yekta Gürsel, Seiji Kawamura, Frederick J Raab, David Shoemaker, Lisa Sievers, Robert E Spero, Kip S Thorne, et al. Ligo: The laser interferometer gravitational-wave observatory. *science*, 256(5055): 325–333, 1992.

[3] Reed W Andrews, Robert W Peterson, Tom P Purdy, Katarina Cicak, Raymond W Simmonds, Cindy A Regal, and Konrad W Lehnert. Bidirectional and efficient conversion between microwave and optical light. *Nature physics*, 10(4):321–326, 2014.

[4] Fabio Ansaloni, Heorhii Bohuslavskyi, Federico Fedele, Torbjørn Rasmussen, Bertram Brovang, Fabrizio Berritta, Amber Heskes, Jing Li, Louis Hutin, Benjamin Venitucci, et al. Gate reflectometry in dense quantum dot arrays. *New Journal of Physics*, 25(3): 033023, 2023.

[5] A. Ashkin. Trapping of atoms by resonance radiation pressure. *Phys. Rev. Lett.*, 40: 729–732, Mar 1978. doi: 10.1103/PhysRevLett.40.729. URL `https://link.aps.org/doi/10.1103/PhysRevLett.40.729`.

[6] Arthur Ashkin. Optical trapping and manipulation of neutral particles using lasers. *Proceedings of the National Academy of Sciences*, 94(10):4853–4860, 1997.

[7] Markus Aspelmeyer, Tobias J. Kippenberg, and Florian Marquardt. Cavity optomechanics. *Rev. Mod. Phys.*, 86:1391–1452, Dec 2014. doi: 10.1103/RevModPhys.86.1391. URL `https://link.aps.org/doi/10.1103/RevModPhys.86.1391`.

[8] Tolga Bagci, Anders Simonsen, Silvan Schmid, Luis G Villanueva, Emil Zeuthen, Jürgen Appel, Jacob M Taylor, A Sørensen, Koji Usami, Albert Schliesser, et al. Optical detection of radio waves through a nanomechanical transducer. *Nature*, 507(7490): 81–85, 2014.

[9] Alberto Beccari, Diego A Visani, Sergey A Fedorov, Mohammad J Bereyhi, Victor Boureau, Nils J Engelsen, and Tobias J Kippenberg. Strained crystalline nanomechanical resonators with quality factors above 10 billion. *Nature Physics*, 18(4):436–441, 2022.

[10] Joerg Bochmann, Amit Vainsencher, David D Awschalom, and Andrew N Cleland. Nanomechanical coupling between microwave and optical photons. *Nature Physics*, 9 (11):712–716, 2013.

[11] Joerg Bochmann, Amit Vainsencher, David D Awschalom, and Andrew N Cleland. Nanomechanical coupling between microwave and optical photons. *Nature Physics*, 9 (11):712–716, 2013.

[12] Daniel Bothner, Shun Yanai, Agustin Iniguez-Rabago, Mingyun Yuan, Ya M Blanter, and Gary A Steele. Cavity electromechanics with parametric mechanical driving. *Nature communications*, 11(1):1589, 2020.

[13] VB Braginski and AB Manukin. Ponderomotive effects of electromagnetic radiation. *Sov. Phys. JETP*, 25(4):653–655, 1967.

[14] VB Braginskiĭ, Anatoli B Manukin, and M Yu Tikhonov. Investigation of dissipative ponderomotive effects of electromagnetic radiation. *Soviet Journal of Experimental and Theoretical Physics*, 31:829, 1970. URL `http://www.jetp.ras.ru/cgi-bin/e/index/e/31/5/p829?a=list`.

[15] Eyal Buks and Michael L Roukes. Electrically tunable collective response in a coupled micromechanical array. *Journal of Microelectromechanical Systems*, 11(6):802–807, 2002.

[16] Jasper Chan, TP Mayer Alegre, Amir H Safavi-Naeini, Jeff T Hill, Alex Krause, Simon Gröblacher, Markus Aspelmeyer, and Oskar Painter. Laser cooling of a nanomechanical oscillator into its quantum ground state. *Nature*, 478(7367):89–92, 2011.

[17] Yiwen Chu, Prashanta Kharel, William H Renninger, Luke D Burkhart, Luigi Frunzio, Peter T Rakich, and Robert J Schoelkopf. Quantum acoustics with superconducting qubits. *Science*, 358(6360):199–202, 2017.

[18] Yiwen Chu, Prashanta Kharel, Taekwan Yoon, Luigi Frunzio, Peter T Rakich, and Robert J Schoelkopf. Creation and control of multi-phonon fock states in a bulk acoustic-wave resonator. *Nature*, 563(7733):666–670, 2018.

[19] AN Cleland and ML Roukes. External control of dissipation in a nanometer-scale radiofrequency mechanical resonator. *Sensors and Actuators A: Physical*, 72(3):256–261, 1999.

[20] AN Cleland, JS Aldridge, DC Driscoll, and AC Gossard. Nanomechanical displacement sensing using a quantum point contact. *Applied Physics Letters*, 81(9):1699–1701, 2002.

[21] Andrew N Cleland and Michael L Roukes. A nanometre-scale mechanical electrometer. *Nature*, 392(6672):160–162, 1998.

[22] Gloria Conte, Leonardo Vicarelli, Simone Zanotto, and Alessandro Pitanti. Mechanical mode engineering with orthotropic metamaterial membranes. *Advanced Materials Technologies*, 7(11):2200337, 2022.

[23] Alessandro Crippa, R Ezzouch, A Aprá, A Amisse, Romain Lavieville, L Hutin, Benoit Bertrand, M Vinet, Matias Urdampilleta, Tristan Meunier, et al. Gate-reflectometry dispersive readout and coherent control of a spin qubit in silicon. *Nature communications*, 10(1):2776, 2019.

[24] Laure Mercier De Lépinay, Benjamin Pigeau, Benjamin Besga, Pascal Vincent, Philippe Poncharal, and Olivier Arcizet. A universal and ultrasensitive vectorial nanomechanical sensor for imaging 2d force fields. *Nature nanotechnology*, 12(2):156–162, 2017.

[25] RD Delaney, MD Urmey, S Mittal, BM Brubaker, JM Kindem, PS Burns, CA Regal, and KW Lehnert. Superconducting-qubit readout via low-backaction electro-optic transduction. *Nature*, 606(7914):489–493, 2022.

[26] Søren Dohn, Silvan Schmid, Fabien Amiot, and Anja Boisen. Position and mass determination of multiple particles using cantilever based mass sensors. *Applied Physics Letters*, 97(4), 2010.

[27] A Eichler, M del Álamo Ruiz, JA Plaza, and A Bachtold. Strong coupling between mechanical modes in a nanotube resonator. *Physical review letters*, 109(2):025503, 2012.

[28] Albert Einstein. On the development of our views concerning the nature and constitution of radiation. *Zeitschrift für Physik*, pages 817–826, 1909. URL `https://einsteinpapers.press.princeton.edu/vol2-trans/393`.

[29] KL Ekinci, XMH Huang, and ML Roukes. Ultrasensitive nanoelectromechanical mass detection. *Applied physics letters*, 84(22):4469–4471, 2004.

[30] Nils J Engelsen, Amirali Arabmoheghi, Mohammad J Bereyhi, Alberto Beccari, Sergey A Fedorov, Yi Xia, Guanhao Huang, Alessio Zicoschi, and Tobias J Kippenberg. Ultralow dissipation mechanical resonators for cavity-free quantum control. In *2023 Conference on Lasers and Electro-Optics (CLEO)*, pages 1–2. IEEE, 2023.

[31] Moritz Forsch, Robert Stockill, Andreas Wallucks, Igor Marinković, Claus Gärtner, Richard A Norte, Frank van Otten, Andrea Fiore, Kartik Srinivasan, and Simon Gröblacher. Microwave-to-optics conversion using a mechanical oscillator in its quantum ground state. *Nature Physics*, 16(1):69–74, 2020.

[32] Mohamed Gad-el Hak. *The MEMS handbook*. CRC press, 2001.

[33] Marc Ganzhorn, Svetlana Klyatskaya, Mario Ruben, and Wolfgang Wernsdorfer. Strong spin–phonon coupling between a single-molecule magnet and a carbon nanotube nanoelectromechanical system. *Nature nanotechnology*, 8(3):165–169, 2013.

[34] Ricardo Garcia and Elena T Herruzo. The emergence of multifrequency force microscopy. *Nature nanotechnology*, 7(4):217–226, 2012.

[35] Thomas Gisler, Mohamed Helal, Deividas Sabonis, Urs Grob, Martin Héritier, Christian L Degen, Amir H Ghadimi, and Alexander Eichler. Soft-clamped silicon nitride string resonators at millikelvin temperatures. *Physical Review Letters*, 129(10):104301, 2022.

[36] M S Hanay, S Kelber, AK Naik, D Chi, S Hentz, EC Bullard, E Colinet, L Duraffourg, and ML Roukes. Single-protein nanomechanical mass spectrometry in real time. *Nature nanotechnology*, 7(9):602–608, 2012.

[37] M Selim Hanay, Scott I Kelber, Cathal D O'Connell, Paul Mulvaney, John E Sader, and Michael L Roukes. Inertial imaging with nanomechanical systems. *Nature nanotechnology*, 10(4):339–344, 2015.

[38] Andrew P Higginbotham, P S Burns, M D Urmey, R W Peterson, N S Kampel, B M Brubaker, G Smith, K W Lehnert, and C A Regal. Harnessing electro-optic correlations in an efficient mechanical converter. *Nature Physics*, 14(10):1038–1042, 2018.

[39] Andrew P Higginbotham, PS Burns, MD Urmey, RW Peterson, NS Kampel, BM Brubaker, G Smith, KW Lehnert, and CA Regal. Harnessing electro-optic correlations in an efficient mechanical converter. *Nature Physics*, 14(10):1038–1042, 2018.

[40] Gavin K Ho, Reza Abdolvand, Abhishek Sivapurapu, Shweta Humad, and Farrokh Ayazi. Piezoelectric-on-silicon lateral bulk acoustic wave micromechanical resonators. *Journal of microelectromechanical systems*, 17(2):512–520, 2008.

[41] Paul Horowitz and Winfield Hill. *The art of electronics*. Cambridge University Press, second edition, 1994.

[42] Jack W Judy. Microelectromechanical systems (mems): fabrication, design and applications. *Smart materials and Structures*, 10(6):1115, 2001.

[43] Vedika Khemani, Rahul Nandkishore, and Shivaji L Sondhi. Nonlocal adiabatic response of a localized system to local manipulations. *Nature Physics*, 11(7):560–565, 2015.

[44] Sang-Gook Kim, Shashank Priya, and Isaku Kanno. Piezoelectric mems for energy harvesting. *MRS bulletin*, 37(11):1039–1050, 2012.

[45] Dustin Kleckner, Brian Pepper, Evan Jeffrey, Petro Sonin, Susanna M Thon, and Dirk Bouwmeester. Optomechanical trampoline resonators. *Optics express*, 19(20): 19708–19716, 2011.

[46] Robert G Knobel and Andrew N Cleland. Nanometre-scale displacement sensing using a single electron transistor. *Nature*, 424(6946):291–293, 2003.

[47] Mykel J. Kochenderfer. *Algorithms for Optimization*. The MIT Press, Cambridge, Massachusetts, 2019.

[48] I Kozinsky, HW Postma, I Bargatin, and ML Roukes. Tuning nonlinearity, dynamic range, and frequency of nanomechanical resonators. *Applied Physics Letters*, 88(25), 2006.

[49] Andrew T. Land, Mitul Dey Chowdhury, Aman R. Agrawal, and Dalziel J. Wilson. Sub-ppm nanomechanical absorption spectroscopy of silicon nitride. *Nano Letters*, 24 (25):7578–7583, 2024. PMID: 38742810.

[50] Benjamin Lassagne, Yury Tarakanov, Jari Kinaret, Daniel Garcia-Sanchez, and Adrian Bachtold. Coupling mechanics to charge transport in carbon nanotube mechanical resonators. *Science*, 325(5944):1107–1110, 2009.

[51] Hoi-Kwan Lau, Alexander Eisfeld, and Jan-Michael Rost. Cavity-free quantum optomechanical cooling by atom-modulated radiation. *Physical Review A*, 98(4):043827, 2018.

[52] Peter Lebedew. Untersuchungen über die druckkräfte des lichtes. *Annalen der Physik*, 311 (11):433–458, 1901. doi: https://doi.org/10.1002/andp.19013111102. URL https://onlinelibrary.wiley.com/doi/abs/10.1002/andp.19013111102.

[53] Arthur W Leissa. *Vibration of plates*, volume 160. Scientific and Technical Information Division, National Aeronautics and, 1969.

[54] Chunyu Li, Erik T Thostenson, and Tsu-Wei Chou. Sensors and actuators based on carbon nanotubes and their composites: a review. *Composites science and technology*, 68(6):1227–1249, 2008.

[55] Liwei Lin, Roger T Howe, and Albert P Pisano. Microelectromechanical filters for signal processing. *Journal of Microelectromechanical systems*, 7(3):286–294, 1998.

[56] Lorenzo Magrini, Philipp Rosenzweig, Constanze Bach, Andreas Deutschmann-Olek, Sebastian G Hofer, Sungkun Hong, Nikolai Kiesel, Andreas Kugi, and Markus Aspelmeyer. Real-time optimal quantum control of mechanical motion at room temperature. *Nature*, 595(7867):373–377, 2021.

[57] I Mahboob, N Perrissin, K Nishiguchi, D Hatanaka, Y Okazaki, A Fujiwara, and H Yamaguchi. Dispersive and dissipative coupling in a micromechanical resonator embedded with a nanomechanical resonator. *Nano letters*, 15(4):2312–2317, 2015.

[58] I Mahboob, R Dupuy, K Nishiguchi, A Fujiwara, and H Yamaguchi. Hopf and period-doubling bifurcations in an electromechanical resonator. *Applied Physics Letters*, 109 (7), 2016.

[59] Pankaj Mehta, Marin Bukov, Ching-Hao Wang, Alexandre GR Day, Clint Richardson, Charles K Fisher, and David J Schwab. A high-bias, low-variance introduction to machine learning for physicists. *Physics reports*, 810:1–124, 2019.

[60] Gerbold C Ménard, Filip K Malinowski, Denise Puglia, Dmitry I Pikulin, Torsten Karzig, Bela Bauer, Peter Krogstrup, and Charles M Marcus. Suppressing quasiparticle poisoning with a voltage-controlled filter. *Physical Review B*, 100(16):165307, 2019.

[61] Mohammad Mirhosseini, Alp Sipahigil, Mahmoud Kalaee, and Oskar Painter. Superconducting qubit to optical photon transduction. *Nature*, 588(7839):599–603, 2020.

[62] Soham Mukhopadhyay, Jorden Senior, Jaime Saez-Mollejo, Denise Puglia, Martin Zemlicka, Johannes M Fink, and Andrew P Higginbotham. Superconductivity from a melted insulator in josephson junction arrays. *Nature Physics*, 19(11):1630–1635, 2023.

[63] Akshay K Naik, MS Hanay, WK Hiebert, XL Feng, and Michael L Roukes. Towards single-molecule nanomechanical mass spectrometry. *Nature nanotechnology*, 4(7):445–450, 2009.

[64] Clark T-C Nguyen. Mems technology for timing and frequency control. *IEEE transactions on ultrasonics, ferroelectrics, and frequency control*, 54(2):251–270, 2007.

[65] Nam-Trung Nguyen, Xiaoyang Huang, and Toh Kok Chuan. Mems-micropumps: a review. *J. Fluids Eng.*, 124(2):384–392, 2002.

[66] E. F. Nichols and G. F. Hull. A preliminary communication on the pressure of heat and light radiation. *Phys. Rev. (Series I)*, 13:307–320, Nov 1901. doi: 10.1103/PhysRevSeriesI.13.307. URL https://link.aps.org/doi/10.1103/PhysRevSeriesI.13.307.

[67] Richard A Norte, Joao P Moura, and Simon Gröblacher. Mechanical resonators for quantum optomechanics experiments at room temperature. *Physical review letters*, 116 (14):147202, 2016.

[68] Preeti Ovartchaiyapong, Kenneth W Lee, Bryan A Myers, and Ania C Bleszynski Jayich. Dynamic strain-mediated coupling of a single diamond spin to a mechanical resonator. *Nature communications*, 5(1):4429, 2014.

[69] Aaron D O'Connell, Max Hofheinz, Markus Ansmann, Radoslaw C Bialczak, Mike Lenander, Erik Lucero, Matthew Neeley, Daniel Sank, H Wang, Martin Weides, et al. Quantum ground state and single-phonon control of a mechanical resonator. *Nature*, 464(7289):697–703, 2010.

[70] GA Peairs, M-H Chou, A Bienfait, H-S Chang, CR Conner, É Dumur, J Grebel, RG Povey, E Şahin, KJ Satzinger, et al. Continuous and time-domain coherent signal conversion between optical and microwave frequencies. *Physical Review Applied*, 14(6):061001, 2020.

[71] AN Pearson, KE Khosla, Matthias Mergenthaler, G Andrew D Briggs, EA Laird, and Natalia Ares. Radio-frequency optomechanical characterization of a silicon nitride drum. *Scientific reports*, 10(1):1654, 2020.

[72] GA Peterson, S Kotler, F Lecocq, K Cicak, XY Jin, RW Simmonds, J Aumentado, and JD Teufel. Ultrastrong parametric coupling between a superconducting cavity and a mechanical resonator. *Physical review letters*, 123(24):247701, 2019.

[73] Christian M Pluchar, Aman R Agrawal, Edward Schenk, and Dalziel J Wilson. Towards cavity-free ground-state cooling of an acoustic-frequency silicon nitride membrane. *Applied Optics*, 59(22):G107–G111, 2020.

[74] Samira Pouyanfar, Saad Sadiq, Yilin Yan, Haiman Tian, Yudong Tao, Maria Presa Reyes, Mei-Ling Shyu, Shu-Ching Chen, and Sundaraja S Iyengar. A survey on deep learning: Algorithms, techniques, and applications. *ACM computing surveys (CSUR)*, 51(5):1–36, 2018.

[75] Denise Puglia, EA Martinez, GC Ménard, A Pöschl, S Gronin, GC Gardner, R Kallaher, MJ Manfra, CM Marcus, Andrew P Higginbotham, et al. Closing of the induced gap in a hybrid superconductor-semiconductor nanowire. *Physical Review B*, 103(23):235201, 2021.

[76] Denise Puglia, Rachel Odessey, Peter S Burn, Niklas Luhmann, Silvan Schmid, and Andrew P Higginbotham. Everyday electromechanics: Capacitive strong coupling to mechanical motion. *arXiv preprint arXiv:2407.15314*, 2024.

[77] Peter Rabl, P Cappellaro, MV Gurudev Dutt, Liang Jiang, JR Maze, and Mikhail D Lukin. Strong magnetic coupling between an electronic spin qubit and a mechanical resonator. *Physical Review B—Condensed Matter and Materials Physics*, 79(4):041302, 2009.

[78] Christoph Reinhardt, Tina Müller, Alexandre Bourassa, and Jack C Sankey. Ultralow-noise sin trampoline resonators for sensing and optomechanics. *Physical Review X*, 6 (2):021001, 2016.

[79] T Rocheleau, T Ndukum, C Macklin, JB Hertzberg, AA Clerk, and KC Schwab. Preparation and detection of a mechanical resonator near the ground state of motion. *Nature*, 463(7277):72–75, 2010.

[80] Massimiliano Rossi, David Mason, Junxin Chen, Yeghishe Tsaturyan, and Albert Schliesser. Measurement-based quantum control of mechanical motion. *Nature*, 563 (7729):53–58, 2018.

[81] Sebastian Ruder. An overview of gradient descent optimization algorithms. *arXiv preprint arXiv:1609.04747*, 2016.

[82] D Rugar and P Grütter. Mechanical parametric amplification and thermomechanical noise squeezing. *Physical Review Letters*, 67(6):699, 1991.

[83] Rishabh Sahu, Liu Qiu, William Hease, Georg Arnold, Yuri Minoguchi, Peter Rabl, and Johannes M Fink. Entangling microwaves with light. *Science*, 380(6646):718–721, 2023.

[84] Adrián Sanz-Jiménez, Jose J Ruz, Eduardo Gil-Santos, Oscar Malvar, Sergio García-López, Priscila M Kosaka, Álvaro Cano, Montserrat Calleja, and Javier Tamayo. Square membrane resonators supporting degenerate modes of vibration for high-throughput mass spectrometry of single bacterial cells. *ACS sensors*, 8(5):2060–2067, 2023.

[85] Masayuki Sato, BE Hubbard, AJ Sievers, B Ilic, DA Czaplewski, and HG Craighead. Observation of locked intrinsic localized vibrational modes<? format?> in a micromechanical oscillator array. *Physical review letters*, 90(4):044102, 2003.

[86] Silvan Schmid, Tolga Bagci, Emil Zeuthen, Jacob M Taylor, Patrick K Herring, Maja C Cassidy, Charles M Marcus, Luis Guillermo Villanueva, Bartolo Amato, Anja Boisen, et al. Single-layer graphene on silicon nitride micromembrane resonators. *Journal of Applied Physics*, 115(5), 2014.

[87] Silvan Schmid, Luis Guillermo Villanueva, and Michael Lee Roukes. *Fundamentals of nanomechanical resonators*, volume 49. Springer, 2016.

[88] Derek K Shaeffer. Mems inertial sensors: A tutorial overview. *IEEE Communications Magazine*, 51(4):100–109, 2013.

[89] Gary A Steele, Andreas K Hüttel, Benoit Witkamp, Menno Poot, Harold B Meerwaldt, Leo P Kouwenhoven, and Herre SJ van der Zant. Strong coupling between single-electron tunneling and nanomechanical motion. *Science*, 325(5944):1103–1107, 2009.

[90] Ilya Sutskever, James Martens, George Dahl, and Geoffrey Hinton. On the importance of initialization and momentum in deep learning. In *International conference on machine learning*, pages 1139–1147. PMLR, 2013.

[91] Felix Tebbenjohanns, M Luisa Mattana, Massimiliano Rossi, Martin Frimmer, and Lukas Novotny. Quantum control of a nanoparticle optically levitated in cryogenic free space. *Nature*, 595(7867):378–382, 2021.

[92] John D Teufel, Tobias Donner, Dale Li, Jennifer W Harlow, MS Allman, Katarina Cicak, Adam J Sirois, Jed D Whittaker, Konrad W Lehnert, and Raymond W Simmonds. Sideband cooling of micromechanical motion to the quantum ground state. *Nature*, 475 (7356):359–363, 2011.

[93] Susan Trolier-McKinstry and Peter Muralt. Thin film piezoelectrics for mems. *Journal of Electroceramics*, 12:7–17, 2004.

[94] Patrick A Truitt, Jared B Hertzberg, CC Huang, Kamil L Ekinci, and Keith C Schwab. Efficient and sensitive capacitive readout of nanomechanical resonator arrays. *Nano letters*, 7(1):120–126, 2007.

[95] Patrick A Truitt, Jared B Hertzberg, CC Huang, Kamil L Ekinci, and Keith C Schwab. Efficient and sensitive capacitive readout of nanomechanical resonator arrays. *Nano letters*, 7(1):120–126, 2007.

[96] Oksana Trushkevych, Vishal Shah, Maksym Myronov, John Halpin, S. Rhead, M. Prest, David Leadley, and Rachel Edwards. Laser-vibrometric ultrasonic characterization of resonant modes and quality factors of ge membranes. *Science and Technology of Advanced Materials*, 15:025004, 04 2014. doi: 10.1088/1468-6996/15/2/025004.

[97] Yeghishe Tsaturyan, Andreas Barg, Eugene S Polzik, and Albert Schliesser. Ultracoherent nanomechanical resonators via soft clamping and dissipation dilution. *Nature nanotechnology*, 12(8):776–783, 2017.

[98] Amit Vainsencher, KJ Satzinger, GA Peairs, and AN Cleland. Bi-directional conversion between microwave and optical frequencies in a piezoelectric optomechanical device. *Applied Physics Letters*, 109(3), 2016.

[99] Bert Voigtländer. *Scanning probe microscopy: Atomic force microscopy and scanning tunneling microscopy*. Springer, 2015.

[100] Kun Wang and CT-C Nguyen. High-order medium frequency micromechanical electronic filters. *Journal of Microelectromechanical systems*, 8(4):534–556, 1999.

[101] Matthew J Weaver, Pim Duivestein, Alexandra C Bernasconi, Selim Scharmer, Mathilde Lemang, Thierry C van Thiel, Frederick Hijazi, Bas Hensen, Simon Gröblacher, and Robert Stockill. An integrated microwave-to-optics interface for scalable quantum computing. *Nature Nanotechnology*, 19(2):166–172, 2024.

[102] Dana Weinstein, Sunil A Bhave, Masahiro Tada, Shun Mitarai, Shinya Morita, and Koichi Ikeda. Mechanical coupling of 2d resonator arrays for mems filter applications. In *2007 IEEE International Frequency Control Symposium Joint with the 21st European Frequency and Time Forum*, pages 1362–1365. IEEE, 2007.

[103] HJR Westra, M Poot, HSJ Van Der Zant, and WJ Venstra. Nonlinear modal interactions in clamped-clamped mechanical resonators. *Physical review letters*, 105(11):117205, 2010.

[104] Ya-Tang Yang, Carlo Callegari, XL Feng, Kamil L Ekinci, and Michael L Roukes. Zeptogram-scale nanomechanical mass sensing. *Nano letters*, 6(4):583–586, 2006.

[105] Chun Zhao, Mohammad H Montaseri, Graham S Wood, Suan Hui Pu, Ashwin A Seshia, and Michael Kraft. A review on coupled mems resonators for sensing applications utilizing mode localization. *Sensors and Actuators A: Physical*, 249:93–111, 2016.

APPENDIX A

Calculating static displacement with Mathematica

```
Lmax = 521 10^-6;
\[CapitalOmega] = Rectangle[{0, 0}, {Lmax, Lmax}];
d = 328 10^-9;
sigmah = 54.96;
epsilon0 = 8.8541878128 10^-12;
epsilonV = epsilon0 (1.3458)^2;
ufun = NDSolveValue[{ sigmah \!\(
\*SubsuperscriptBox[\(\[Del]\), \({x, y}\), \(2\)]\(u[x, y]\)\) ==
     epsilonV /(2  d^2) - (u[x, y] epsilonV)/d^3,
        DirichletCondition[
          u[x, y] == 0 ,
     Abs[x] == 0 || Abs[y] == 0 || Abs[y] == Lmax || Abs[x] == Lmax]},
      u, {x, y} \[Element] \[CapitalOmega]];
c = ColorData["Rainbow"];
Plot3D[ufun[x, y], {x, y} \[Element] \[CapitalOmega],
 ColorFunction -> "TemperatureMap", AspectRatio -> Automatic,
 PlotPoints -> 100, MaxRecursion -> 8, TicksStyle -> Large,
 ColorFunction -> Function[{x, y, z}, #[z]]]
Plot[ufun[x, y] /. x -> Lmax/2, {y, 0, Lmax}, PlotPoints -> 100];
```

APPENDIX B

Sample parameters

Three samples were measured to produce the data for the Chapter 6. The geometric parameters of the samples are as follows:

parameter	Sample 1	Sample 2	Sample 3
L (μm)	514	520	511
d (nm)	226	321	607
m (ng)	185	189	182
t_{metal} (nm)	28	28	28
$\Omega_0/2\pi$ (kHz)	500	380	389
κ_{in} (Hz)	36±8	5±2	9±6

Table B.1: Geometric and resonance parameters of the three samples used in Chapter 6. For geometric parameters, L is the membrane side length, d is the separation distance of the top and bottom chip, m is the membrane mass, and t_{metal} is the deposited metal thickness. For resonance parameters, $\Omega_0/2\pi$ is the resonant frequency and κ_{in} is the internal dissipation calculated at zero effective voltage.